Analytical and modelling strategies for thermal histories from in situ (U-Th-Sm)/He data of single apatites

Ann-Kathrin Maier[2,1], Christoph Glotzbach[1], Sarah Falkowski[3,1]

[1]Department of Geosciences, University of Tübingen, 72076 Tübingen, Germany
[2]Institute of Seismology, Department of Geosciences and Geography, University of Helsinki, Helsinki, 00014, Finland
[3]School of Geographical & Earth Sciences, University of Glasgow, Glasgow, G12 8RZ, UK

Correspondence to: Ann-Kathrin Maier (ann-kathrin.maier@helsinki.fi)

Abstract. (U-Th-Sm)/He is a thermochronometric method used to reconstruct the rates and timing of geological processes. Recent developments in analytical approaches, specifically laser ablation (in situ) measurements, allow quantifying the distribution of parent isotopes (U, Th, and, in apatites, Sm) and decay products (^{4}He) within individual mineral grains. This is particularly important to understand potential date over-dispersion, which can arise from the heterogeneous distribution of parent isotopes, and to develop thermal history modelling for single-grain (U-Th-Sm)/He techniques.

We build on previous studies and combine in situ ^{4}He concentration profile measurements with parent nuclide distribution mapping in natural apatites to explore analytical and modelling strategies for single-grain thermal history reconstructions. Specifically, we investigate the effects of laser ablation spot size, the number and location of ablation spots in a grain, and grain size on data resolution and suitability for thermal history modelling. In doing so, we introduce the calculation of C_{aw}, which is the concentration of parent nuclides at each ablation site weighted by alpha-particle stopping distances to account for the redistribution of ^{4}He in the crystal from high-energy alpha decay. We present stacked U, Th, and Sm maps measured at different ablation depths in two apatite grains from South Germany (one with homogeneous and one with zoned parent isotope distribution) and one apatite from the McClure Mountain Syenite age standard. Furthermore, we show in situ ^{4}He profiles of the two South German apatites and inversions for thermal histories. Our results indicate that, for our study and instrument set-up (a RESOchron system (Applied Spectra) consisting of a He-line and an excimer laser), four to six spot measurements at various distances from the grain rim enable measuring an in situ ^{4}He profile. We tested different laser ablation spot sizes (10 –30 µm) in grains with a range of ^{4}He concentrations and (U-Th-Sm)/He dates (16 to ~200 Ma) and determined that the optimal spot diameter for in situ ^{4}He profile measurements for apatite grains with (U-Th-Sm)/He dates as young as 16 Ma is 20–30 µm. Additionally, with an ablation spot diameter of 20 µm, a six-spot in situ ^{4}He profile requires a minimum grain diameter (measured perpendicular to the c-axis) of 145 µm. Combined with information from detailed parent nuclide maps, the in situ ^{4}He profiles offer a possibility to reconstruct the thermal histories of single grains, potentially including zoned and irregularly shaped crystals.

1 Introduction

Temperature-sensitive geologic processes, including mountain building, fault activity, landscape and sedimentary basin evolution, and ore deposit formation can be constrained with low-temperature thermochronology techniques such as (U-Th-Sm)/He (e.g., Ehlers, 2005; McInnes et al., 2005). Due to its comparatively low nominal closure temperature of ~70 °C (e.g., Wolf et al., 1996, 1998; Shuster et al., 2006), apatite (U-Th-Sm)/He (AHe) is particularly well-suited for constraining the thermal history of such upper crustal processes. Fundamentally, AHe is based on the competing ingrowth and thermally activated diffusive loss of alpha-particles (^{4}He) from the radioactive decay of the uranium and thorium decay chains and samarium in the crystal lattice. Diffusive loss occurs over a specific temperature range, the helium partial retention zone (e.g., Zeitler et al., 1987; Farley, 2002; Fitzgerald et al., 2006). Apart from apatite, other minerals incorporating significant amounts of uranium and thorium and harbouring characteristic temperature sensitivities, such as zircon, titanite, hematite and monazite, can also be used for (U-Th-Sm)/He dating (e.g., Ault et al., 2019).

The amount of helium retained in a crystal is a function of the time-temperature evolution of a rock sample and the crystal-specific properties affecting the diffusivity, including (1) the grain size and geometry determining the diffusion domain and the alpha-particle ejection at the grain boundary, (2) the concentration of effective uranium (eU=U+0.235×Th) representative of the extent of self-irradiation-induced crystal lattice defects (i.e., radiation damage), (3) the presence of fluid and mineral inclusions and phases around the crystal contributing potential excess ^{4}He, and (4) the distribution of parent nuclides (e.g., Farley et al., 1996, 2011; Reiners and Farley, 2001; Shuster et al., 2006; Vermeesch et al., 2007; Spiegel et al., 2009; Gautheron et al., 2012; Anderson et al., 2017). A meaningful geological interpretation of (U-Th-Sm)/He dates thus requires understanding and accounting for these aspects.

Beyond that, reconstructing thermal histories from (U-Th-Sm)/He data is challenging due to the inability to constrain cooling histories solely based on a single (U-Th-Sm)/He date, as a date is non-unique regarding possible time-temperature paths (e.g., Shuster and Farley, 2004). Researchers thus developed different strategies, such as the use of crystals with varying kinetic properties (i.e., grains of varying sizes, radiation damage, or grain fragments), the combination of different thermochronometer systems, and the analysis of samples taken along a quasi-vertical elevation profile to overcome this limitation (e.g., Reiners and Farley, 2001; Fitzgerald et al., 2006; Flowers, 2009; Flowers and Kelley, 2011; Beucher et al., 2013; Brown et al., 2013). In addition to such approaches involving multiple mineral grains, the shape of a single grain's diffusion profile, acquired through proton irradiation and subsequent stepwise degassing, is exploited in the ^{4}He/^{3}He method with the rationale that a ^{4}He profile reflects the duration of active diffusion a crystal experienced and, hence, its possible thermal history (Shuster and Farley, 2004). While, for example, a more rounded profile towards the grain rim would indicate slow cooling, a uniform ^{4}He distribution would be produced by faster cooling (Shuster and Farley, 2004). A heterogeneous parent radionuclide distribution in a grain may complicate the interpretation of ^{4}He concentration profiles (e.g., Farley et al., 2011).

For thermal modelling, it is essential to characterise the spatial distribution of ^{4}He and its parent radionuclides, and to understand sources of possible (U-Th-Sm)/He date dispersion, such as parent nuclide zonation (e.g., Farley et al., 2011;

Vermeesch et al., 2012; Danišík et al., 2017; Idleman et al., 2018; Sousa et al., 2024). The in situ technique to determine both helium and trace element content via laser-ablation promises new insights compared to more established whole-grain protocols (e.g., Gautheron et al., 2021), where the spatial relationship between parent nuclides and decay products in single grains generally remains unquantified (Boyce et al., 2006; Vermeesch et al., 2012, 2023; Danišík et al., 2017; Glotzbach and Ehlers, 2024). Not least, in situ mapping of parent nuclides and ^{4}He allows the determination of a single grain's possible thermal history. Danišík et al. (2017) demonstrated this by assessing the spatial relationship of uranium, thorium, and helium in zircons by µm-scale laser ablation inductively coupled plasma mass spectrometry (LA-ICP-MS) element mapping and conversion of their detailed 2D maps into 1D concentration profiles to then invert for a possible single-grain thermal history. Recently, Glotzbach and Ehlers (2024) suggested optimised strategies for the reconstruction of cooling histories from in situ measurements based on synthetic data modelling and the incorporation of in situ (U-Th-Sm)/He adapted helium production-ejection-diffusion models. They suggested using either in situ measurements of multiple grains of varying size or eU, similar to the whole-grain method, or multiple in situ spot measurements along a core-to-rim profile in a single grain. However, they did not test their strategies on natural samples.

In this study, we expand on the work by Danišík et al. (2017) and Glotzbach and Ehlers (2024) and test whether it is possible to obtain reliable single-grain helium concentration profiles from in situ ^{4}He measurements and combine them with parent nuclide maps for cooling history inversion. We explore analytical and thermal modelling strategies for best results using natural samples from South Germany with homogeneous and heterogeneous radionuclide distributions and a large and clear apatite from the McClure Mountain Syenite (Colorado, USA). Specifically, we examine the number of ablation spots needed to retrieve an interpretable ^{4}He profile and evaluate limitations on grain size and ablation spot location and size.

2 Methods

This section presents our analytical workflow (Fig. 1), including the ^{4}He profile and parent nuclide measurement protocols, data visualisation, and thermal history modelling strategy. As detailed descriptions of laser-ablation in situ (U-Th-Sm)/He analyses are provided elsewhere (e.g., Boyce et al., 2006; Horne et al., 2016), we focus on the specifics of our procedure. Technical details of (U-Th-Sm)/He analysis in our laboratory, error propagation and age calculation are available in the Supplementary Material (S1).

2.1 Sample selection

We analysed apatites extracted from different lithologies in South Germany and the McClure Mountain Syenite (U-Pb age standard 523.5 ± 1.5 Ma, Schoene & Bowring, 2006) (Table 1). The rationale for sample selection was to choose samples comprising large pristine crystals with a simple cooling history for method validation, along with a more complex sample for testing the method's limitations. The obvious choice for validation material, the Fish Canyon Tuff (FCT) and Durango standards, were not suitable for our approach as the crystals available at our laboratory were either too small (FCT) or too large

(Durango) to be analysed within a reasonable investment of resources. In addition, FCT bears the risk of significant zonation (cf., Pickering et al. 2020). Hence, we substituted those standards with Apatite-URG, a sample sourced from a Miocene foiditic tuff with an independently determined U-Pb age (Table 1; Binder et al., 2023) and an abundance of reasonably large euhedral and clear crystals. Given its geological context, Apatite-URG has a simple expected cooling history, making it a good validation material. Equally, the McClure Mountain Syenite standard was chosen for its clear and euhedral crystals. The sample Apatite-BaF, on the other hand, was selected for its complexity to test the limitations of our approach.

2.2 Sample preparation

Datable crystals were selected based on the criteria for whole-grain analyses, i.e., no visible inclusions, fractures, defects, and rounded or broken edges and tips, and a diameter larger than 60 µm (e.g., Farley, 2002), and photographed parallel and perpendicular to the c-axis following the 3D-He protocol of Glotzbach et al. (2019) to record the grain geometry information needed for thermal history modelling. Afterwards, the grains were embedded in a Teflon sheet with their c-axis parallel to the mount surface. The Teflon mounting process exposed the grains to 300°C for 2 minutes on a hotplate. For this heating temperature and duration, helium loss from the grains is negligible (see Supplementary S1.1). After embedding, the mount was ground down and polished to expose internal grain surfaces. The amount of material removed was tracked with reference glass beads of known diameter, as described by Pickering et al. (2020). Imaging the uncoated mount with a tabletop scanning electron microscope (SEM) at a voltage of 15 kV, an emission current of 40.3 µA, filament power of 4.46 W, and a dwell time of 200 ns before laser ablation analysis did not reveal internal zonation in any of the chosen crystals (SEM images are shown in Section 3.2). Note that an SEM analysis with these settings is not expected to cause helium loss from the embedded and exposed grains (cf., Shan et al., 2013).

Table 1: Sample information

Sample	Lithology and crystallisation age	Location	Longitude[a]	Latitude[a]
Apatite-URG	Foiditic tuff (16.75±0.84 Ma, Binder et al., 2023)	Herbolzheim (Upper Rhine Graben)	7.779325	48.2319861
Apatite-BaF	Biotite-rich coarse granite (Variscan)	Prenning (Bavarian Forest)	12.939167	49.016389
Apatite-McClure	Hornblende-biotite syenite (523.5±1.5 Ma, Schoene & Bowring, 2006)	Wet Mountains (Colorado)	-105.483333[b]	38.35[b]

[a] The coordinates (in decimal degree) are referenced to WGS84.
[b] These are approximate coordinates based on the original sample locality reported in Alexander et al. (1978).

2.3 In situ helium profile measurements

We acquired ^{4}He concentration profiles from multiple in situ ^{4}He spot measurements along several c-axis perpendicular and one c-axis parallel traverses through single crystals (Fig. 1) to evaluate the influence of the measurement location, the consistency of the results, and potential effects of parent nuclide heterogeneities. This resulted in 28–38 individual ablation sites per crystal (Table 2). While the c-axis perpendicular profiles were acquired for thermal modelling, the c-axis parallel profiles were measured to verify the ^{4}He concentration's consistency in the grain along this direction.

The in situ ^{4}He measurements were conducted with a RESOchron system (Applied Spectra) consisting of a He-line and an excimer laser at the University of Tübingen, Germany. All analysed grains were ablated for 8 s with a laser pulse frequency of 10 Hz and a laser fluence of 2 J cm^{-2}. The laser ablation spots, sized 10–30 µm in diameter, were spaced 3–5 µm apart to avoid signal smearing and mixing (Fox et al., 2017). The laser spot sizes were chosen individually for each grain and set as small as possible to ensure acceptable helium signals of three standard deviations above the blank level (Table 2). Line blanks were recorded regularly in the ablation sequence and were in the order of 2E7 atoms (~0.0007 ncc). Blank correction, Q-shot interpolation to account for instrumental drift, and ^{4}He content calculation (Supplementary S1.2) were performed using in-house software.

For successful ^{4}He measurements, standard deviations after blank correction ranged from 6–15% (Table 2). After ^{4}He measurements, the surface topography of the analysed grains was imaged using a confocal laser-scanning microscope (Zeiss LSM 900) to determine the ablation pit dimensions. Based thereon, the ablation pit volumes were obtained in the Zeiss Confomap software and used to calculate pit-volume normalised ^{4}He concentrations. For Apatite-BaF and Apatite-McClure, we used the mean pit volume to calculate the ^{4}He concentrations due to a large spread in measured pit volumes (see Section 4.3 for limitations of pit volume measurements). Detailed pit volumes for individual ablation spots are listed in Table 3. Mean pit volumes in the analysed apatites ranged from 310 µm^3 ± 10 % to 4240 µm^3 ± 4 % (1 SD; Table 2).

2.4 Parent nuclide mapping

Following ablation for ^{4}He measurements, we performed detailed parent nuclide mapping to garner the necessary information for thermal modelling and to assess the possible effect of U, Th, and Sm heterogeneities on the measured ^{4}He distribution following the example of Danišík et al. (2017).

Prior to parent nuclide measurements, the grains were re-polished for 3.5 hours on a polishing machine at intervals of 4 to 20 minutes, with a decreasing force from 20 N to 10 N, to remove the helium ablation pits and create an even surface for U, Th, and Sm distribution mapping. Starting with an even surface makes spatially correlating measurements at different recorded horizontal locations in the grain easier, as the depth component can be assumed to be consistent. To avoid polishing more than necessary, the state of removal was checked multiple times during the process, and polishing was stopped when visible pit traces had been completely removed. Based on the measured ^{4}He ablation pit depths, repolishing removed a maximum of 10 µm.

The LA-ICP-MS measurements were conducted on an evenly spaced grid of non-overlapping spots (Fox et al., 2017) across the smoothly re-polished grain surfaces, following ablation for ^{4}He measurements, with a spot diameter of 24 µm and a spot depth of approximately 24 µm. The ablation time was 12 s with a laser fluence of 3 J cm^{-2} and a pulse frequency of 20 Hz. We used NIST612 and the Durango apatite age standard (AHe age 31.02±1.01 Ma, McDowell et al., 2005) as reference material for apatite in the standard bracketing approach to estimate trace element concentrations (Paton et al., 2010). Removal of outliers (per default all measured counts per second (CPS) more than three standard deviations away from a running mean), background correction, and trace element concentration calculation were performed with an in-house MATLAB app (ESD-U-Pb).

To construct stacked 2D maps of parent nuclide distributions from deep ablation spots on just one internal surface, we used the "downhole" time-resolved measurements and the approximate ablation time-depth relationship. The latter was determined by measuring pit depths corresponding to 2–18 s ablation times in spare apatite grains of the same samples. The resulting time-depth relationship was approximately linear, with an ablation rate of ~2 µm s^{-1}.

Finally, we computed sub-ablation-spot resolution U, Th, and Sm distribution maps from neighbouring spot measurements using the regularised linear least squares MATLAB code by Fox et al. (2017). Such a regularised inversion requires balancing model smoothness and complexity by choosing an adequate regularisation parameter or smoothness constraint λ. The smoothness constraint controls the influence the penalty term for model complexity has on the inversion result. A too-large smoothness constraint leads to retrieving parent nuclide maps that are too smooth and do not capture the underlying true concentration variations. Conversely, if the regularisation parameter is too small, the inversion solution will be dominated by data errors, and every small concentration change (noise) will be matched. Following Fox et al. (2017), we chose the smoothness constraint based on qualitative information from SEM and the L-curve criterion (e.g., Hansen and O'Leary, 1993). The L-curve is a log-log plot of the residual against the norm of the regularised solution parameterised by the smoothness constraint, which is often L-shaped. The idea is to choose the smoothness constraint that corresponds to the corner of the "L". In this way, we computed 2D parent nuclide distribution maps with a resolution of 10x10 µm (Apatite-URG) and 5x5 µm (Apatite-BaF, Apatite-McClure) for each recorded laser penetration depth. We stacked those map slices to display a pseudo-3D section through the analysed part of the grain (Section 3.3).

Table 2: ^{4}He- and trace element measurement details

		^{4}He					Trace elements	
Sample	Grain radius [µm]	Number of ablation spots	Ablation spot diameter [µm]	Mean pit depth ± 1 SD [µm]	Mean ablation pit volume ± 1 SD [µm]	1 SD ^{4}He[a] [%]	Number of ablation spots	Ablation spot diameter, pit depth[b] [µm]
Apatite-URG	175	32	30	8.1 ± 0.6	4240 ± 170	<15	356	24, 24
Apatite-BaF	89	28	20	7.9 ± 0.9	1550 ± 140	<6	90	24, 24
Apatite-McClure	75	38	10	9.7 ± 0.3	310 ± 30	>40	84	24, 24

[a] This is the ^{4}He measurement uncertainty after blank correction.

[b] Pit depths for trace element measurements are calculated values derived from the established ablation-time-depth relationship (Section 2.6). SD stands for standard deviation.

2.5 Alpha-stopping distance weighted parent nuclide concentration C_{aw}

As the in situ ^{4}He (spots along profiles) and parent nuclide measurements (spots for 2D maps) do not correspond to the same location in the grain in our procedure (Fig. 1), we had to match the separate U, Th, Sm, and ^{4}He measurements for thermal modelling. For this purpose, we determined an alpha-stopping distance weighted parent nuclide concentration (C_{aw}, **C**oncentration **a**lpha-**w**eighted) at each helium ablation site. Although other options to make information from 2D parent nuclide maps usable for thermal modelling already exist, for example, calculating 1D equivalent-sphere geometry concentration profiles (e.g., Farley et al., 2011; Danišík et al., 2017), we introduce this alpha-stopping distance weighted parent nuclide concentration because it allows us to account for the emission and redistribution of ^{4}He (alpha particles) from the decay site during high-energy decay. Since ^{4}He measured in a spot is the result of the parent nuclides that surround it within the alpha-stopping distance reach (e.g., Farley et al., 2010), we determined C_{aw} from the distribution of parent nuclides in each ^{4}He spot's periphery . First, we calculated the mean U, Th, and Sm concentrations around the centre point of each ^{4}He measurement spot for spheres with radii corresponding to all possible alpha-stopping distances (between ~6 and 40 µm, Ketcham et al., 2011). Then, we summed the mean parent nuclide concentration for each stopping distance weighted by its contribution to ^{4}He production .

$$C_{aw} = \sum_j^m f_j \frac{\sum_{i=1}^n c_{i,j}}{n} \qquad \text{(Eq. 1)}$$

In Equation 1, c is the parent nuclide concentration within a certain stopping distance, n is the number of concentration measurements, m is the number of stopping distances, and f is the weight for the contribution to the production of ^{4}He.

The C_{aw} calculation is based on the available 3D information on the parent nuclide distribution and is, hence, constrained by the resolution and accuracy of the measured parent nuclide maps. It thus depends on the number of mapped grain slices, the accuracy of the ablation time-depth relationship (Section 2.4), and the fact that information of the top half of the grain is inevitably lost from grinding it down. Due to the latter, we made the following simplifying assumptions. (1) Grains are mirror-symmetrical about the polished internal grain surface, (2) helium and trace elements were measured in the same plane, and (3) where there is a lack of 3D data, we assume the same concentration as for the closest measurement (interpolation) point. Finally, we chose not to calculate C_{aw} for ^{4}He ablation spots with centres <40 µm to the grain rim (maximum alpha-stopping distance; Ketcham et al., 2011) because at the grain rim, ^{4}He is not only redistributed, but can also be ejected and lost or implanted (e.g., Farley et al., 1996). This restricts the ablation spots usable for thermal history inversion to those > 40 µm from the grain rim. However, it does not imply that spots < 40 µm from the grain rim should not be measured. On the contrary, they provide crucial information about the ^{4}He profile's shape, and they are a vital part in assessing the quality of the inversion results through misfit calculation between the modelled and measured ^{4}He profiles.

2.6 Thermal history modelling

The shape of a ^{4}He concentration profile in a grain is largely a function of the duration of active diffusion and, thus, thermal history (Shuster and Farley, 2004). We can, therefore, reconstruct thermal histories by inverting the in situ ^{4}He profile

measurements and the corresponding alpha-stopping distance weighted parent nuclide concentrations (C_{aw}). We applied the modelling technique outlined by Glotzbach and Ehlers (2024), which allows predicting the ^{4}He concentrations at specific locations in a c-axis symmetric grain, assuming a cylindrical grain geometry and considering the full range of alpha-stopping distances. Glotzbach and Ehlers's (2024) MATLAB code is an adjustment of the radiation damage accumulation and annealing models (RDAAM, Flowers et al. (2009), and ZrDAAM, Guenthner et al. (2013)) implemented in HeFTy (Ketcham, 2005; Ketcham et al., 2018; Ketcham, 2024). The RDAAM (apatite) and ZrDAAM (zircon) models treat ^{4}He diffusion in a grain as a function of accumulated self-irradiation damage and related diffusivity variations over the grains' thermal evolution (Flowers et al., 2009; Guenthner et al., 2013). Using the approach of Glotzbach and Ehlers (2024), helium production and diffusion was calculated for 5000 (Apatite-URG) and 10000 (Apatite-BaF) random time-temperature paths based on the horizontal and vertical distance of a ^{4}He ablation spot centre to the grain rims, the ^{4}He pit depth, the grain radius, and the U, Th, Sm, and ^{4}He concentrations. Each path's goodness of fit (GOF) was evaluated as in HeFTy, where a GOF of 0.05 corresponds to acceptable time-temperature paths passing the 95% confidence test and a GOF of 0.5 (statistical precision limit) to good paths (Ketcham, 2005; Ketcham, 2024).

The paths with the highest GOF were selected to forward-model the corresponding ^{4}He profiles. Our forward models merge two core-rim profiles to avoid information loss for heterogeneous grains with asymmetric ^{4}He profiles. The profile merging expresses itself in a small ^{4}He concentration jump at the centre of the grain that arises from the exclusion of the centre-most point from one of the two merged core-rim profiles, to prevent it from being defined twice.

The misfit m between modelled and measured ^{4}He profiles was calculated as

$$m = \sqrt{\sum_{i=1}^{n} \frac{r_i^2}{\sigma_i^2}} \qquad \text{(Eq. 2)}$$

with r_i being the residual between measured and modelled concentration at the ith ^{4}He spot and σ_i being the measurement uncertainty, to narrow down the possible time-temperature paths and to assess the quality of the inversion results. This way, a limited number of plausible cooling histories is computed for a grain, which can be interpreted in the geological context.

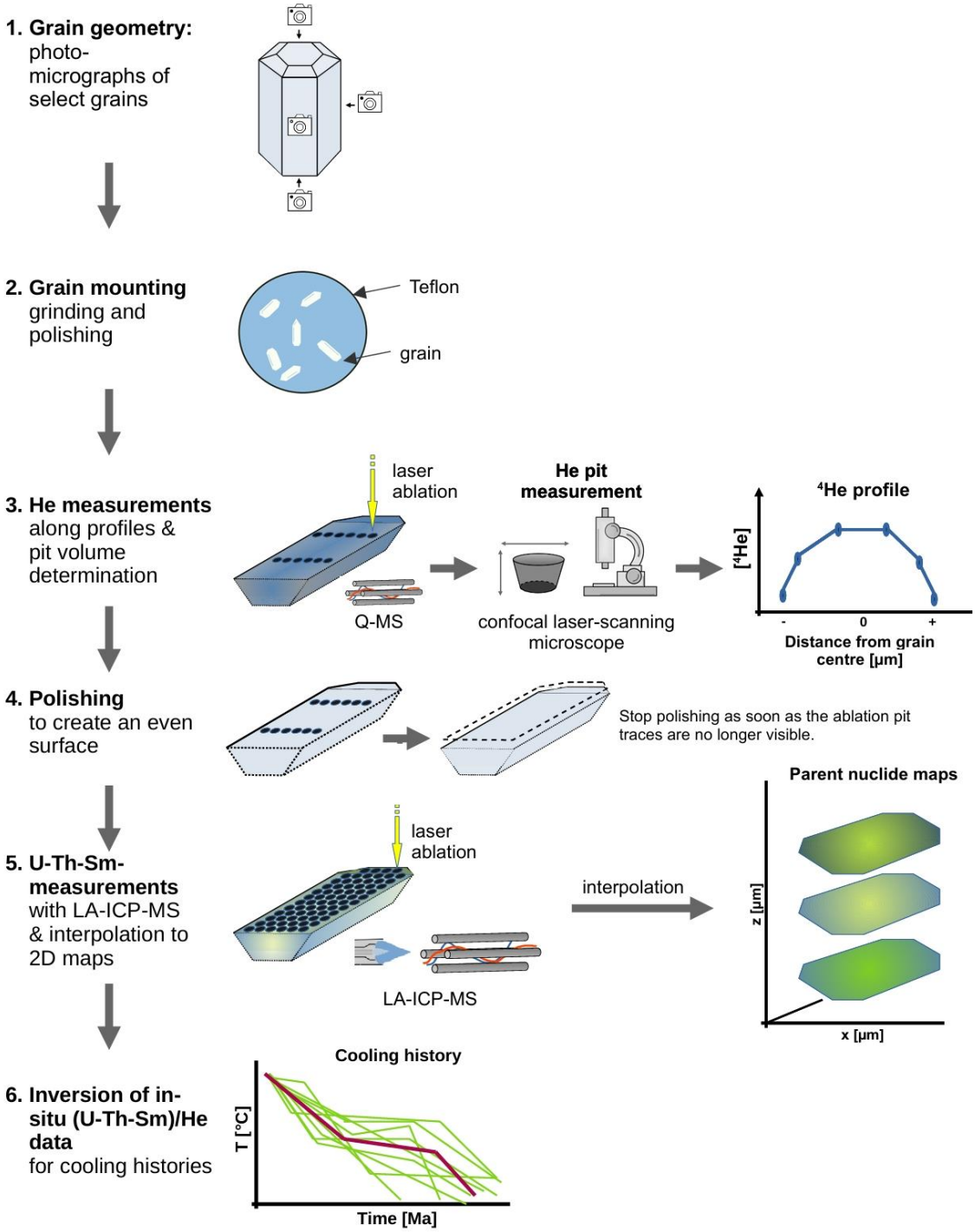

Figure 1: Schematic depiction of the analytical protocol for in situ ^{4}He profile measurements and parent nuclide mapping to reconstruct thermal histories of single grains. Q-MS: quadrupole mass spectrometer; LA-ICP-MS: laser ablation inductively coupled plasma mass spectrometry.

3 Results

3.1 In situ ^{4}He concentrations and uncertainties

The grains examined in this study span a broad range of ^{4}He concentrations and associated uncertainties, highlighting differences in parent nuclide concentration and cooling history. In situ ^{4}He concentrations range from $1.7\times10^{15} \pm 2.2\times10^{14}$ at g^{-1} to $2.1\times10^{15} \pm 3.0\times10^{14}$ at g^{-1} for Apatite-URG and $1.1\times10^{16} \pm 1.2\times10^{15}$ at g^{-1} to $2.4\times10^{16} \pm 2.4\times10^{15}$ at g^{-1} for Apatite-BaF. Corresponding uncertainties after blank correction and pit volume determination are <15% and <10%, respectively (Table 2). The Apatite-McClure sample with ^{4}He concentrations of $2.8\times10^{15} \pm 5.0\times10^{15}$ at g^{-1} to $8.5\times10^{15} \pm 2.5\times10^{15}$ at g^{-1} has a comparatively high uncertainty of >40% after blank correction stemming from a too low ablated volume and ^{4}He signal.

Table 3: ^{4}He and alpha-stopping distance weighted parent nuclides concentrations (C_{aw})

Spot	Pit volume [µm^3]	^{4}He [at g^{-1}]	^{4}He SD [at g^{-1}]	^{238}U C_{aw} ± 1SD [ppm] [a]	^{232}Th C_{aw} ± 1SD [ppm] [a]	^{147}Sm C_{aw} ± 1SD [ppm] [a]	Distance to grain boundary [µm] [b]	in situ AHe date ± 1SD [Ma] [c]
Ap-URG_1	4011	2.13×10^{15}	1.93×10^{14}	7.4 ± 1.0	107 ± 10	238 ± 33	59	20.0 ± 2.3
Ap-URG_2	4121	1.95×10^{15}	1.70×10^{14}	8.1 ± 0.8	109 ± 10	230 ± 49	98	17.7 ± 1.9
Ap-URG_3	4215	1.84×10^{15}	2.08×10^{14}	7.9 ± 0.8	107 ± 9	136 ± 19	135	17.1 ± 2.1
Ap-URG_4	4146	1.98×10^{15}	3.15×10^{14}	8.3 ± 1.4	116 ± 19	217 ± 27	133	17.3 ± 3.7
Ap-URG_5	3995	2.05×10^{15}	2.70×10^{14}	7.1 ± 0.7	98 ± 9	132 ± 10	93	20.9 ± 3.1
Ap-URG_6	4150	2.02×10^{15}	3.85×10^{14}	7.4 ± 1.2	107 ± 16	259 ± 27	119	19.1 ± 4.2
Ap-URG_7	4324	1.70×10^{15}	2.69×10^{14}	8.3 ± 0.9	113 ± 11	160 ± 11	158	15.2 ± 2.5
Ap-URG_8	4442	1.74×10^{15}	2.73×10^{14}	8.2 ± 1.5	118 ± 23	146± 8	117	15.3 ± 3.5
Ap-URG_9	4075	1.84×10^{15}	2.62×10^{14}	7.8 ± 1.3	116 ± 25	166 ± 11	79	16.7 ± 4.0
Ap-URG_12	4420	1.95×10^{15}	1.34×10^{14}	9.1 ± 1.8	117 ± 14	123 ± 15	164	16.3 ± 2.0
Ap-URG_15	4295	1.92×10^{15}	2.86×10^{14}	7.5 ± 0.9	107 ± 12	140 ± 26	175	18.1 ± 3.0
Ap-URG_16	4217	1.78×10^{15}	2.29×10^{14}	8.0 ± 1.4	108 ± 16	199 ± 71	174	16.0 ± 2.8
Ap-URG_17	4260	1.85×10^{15}	2.63×10^{14}	8.1 ± 0.9	111 ± 14	151 ± 21	173	16.7 ± 2.9
Ap-URG_18	3896	2.00×10^{15}	3.33×10^{14}	8.0 ± 1.2	108 ± 16	184 ± 5	169	18.5 ± 3.8
Ap-URG_19	4390	1.82×10^{15}	2.98×10^{14}	7.6 ± 1.1	101 ± 15	149 ± 9	165	17.9 ± 3.7

Ap-URG_20	4287	1.84×10^{15}	3.10×10^{14}	7.5 ± 0.9	99 ± 10	122 ± 10	161	18.2 ± 3.3
Ap-URG_21	4265	1.74×10^{15}	2.11×10^{14}	8.0 ± 1.2	106 ± 17	140 ± 23	156	16.2 ± 3.0
Ap-URG_22	4526	1.69×10^{15}	2.21×10^{14}	8.0 ± 1.0	108 ± 13	199 ± 68	153	15.5 ± 2.3
Ap-URG_28	4225	2.04×10^{15}	2.48×10^{14}	7.9 ± 1.3	113 ± 15	199 ± 7	48	18.3 ± 2.9
Ap-URG_29	4589	1.85×10^{15}	2.16×10^{14}	9.5 ± 1.7	114 ± 19	165 ± 6	86	15.9 ± 2.8
Ap-URG_30	4373	1.89×10^{15}	2.22×10^{14}	10.3 ± 1.9	123 ± 18	169 ± 36	126	14.9 ± 2.5
Ap-URG_31	4203	1.92×10^{15}	2.37×10^{14}	7.8 ± 0.9	106 ± 11	153 ± 4	148	17.9 ± 2.7
Ap-URG_32	4294	1.87×10^{15}	2.77×10^{14}	7.4 ± 0.8	104 ± 10	154 ± 4	108	17.8 ± 3.0
Ap-BaF_1	1418	1.26×10^{16}	1.34×10^{15}	-	-	-	42	-
Ap-BaF_2	1387	1.56×10^{16}	1.67×10^{15}	43 ± 6	15 ± 4	516 ± 101	66	101.4 ± 17.0
Ap-BaF_3	1489	1.86×10^{16}	1.86×10^{15}	46 ± 5	20 ± 2	703 ± 182	60	111.4 ± 15.9
Ap-BaF_4	1479	1.48×10^{16}	1.54×10^{15}	30 ± 5	-	595 ± 191	35	-
Ap-BaF_7	1796	1.90×10^{16}	1.88×10^{15}	50 ± 3	19 ± 2	606 ± 56	84	104.7 ± 10.9
Ap-BaF_9	1731	1.67×10^{16}	1.78×10^{15}	52 ± 4	22 ± 4	709 ± 36	86	88.0 ± 11.9
Ap-BaF_11	1418	1.64×10^{16}	1.85×10^{15}	50 ± 4	22 ± 4	589 ± 79	87	90.5 ± 11.6
Ap-BaF_14	1566	1.82×10^{16}	1.72×10^{15}	60 ± 4	25 ± 2	614 ± 93	88	83.2 ± 9.6
Ap-BaF_17	1621	1.54×10^{16}	1.65×10^{15}	–	–	–	38	–
Ap-BaF_18	1603	2.24×10^{16}	2.12×10^{15}	32 ± 6	16 ± 2	496 ± 31	64	125.8 ± 15.8
Ap-BaF_19	1806	2.18×10^{16}	2.30×10^{15}	50 ± 6	23 ± 4	701 ± 69	60	126.8 ± 15.8
Ap-BaF_20	1757	1.72×10^{16}	1.92×10^{15}	(29 ± 5)	(11 ± 3)	(459 ± 38)	33	(162.3 ± 29.0)
Ap-BaF_21	1604	1.07×10^{16}	1.17×10^{15}	-	-	-	10	-
Ap-BaF_22	1448	1.77×10^{16}	1.87×10^{15}	31 ± 7	-	594 ± 186	36	-
Ap-BaF_23	1488	2.36×10^{16}	2.35×10^{15}	50 ± 10	21 ± 5	664 ± 152	62	133.3 ± 27.1
Ap-BaF_24	1445	1.59×10^{16}	1.62×10^{15}	50 ± 5	17 ± 4	518 ± 23	61	90.2 ± 12.9
Ap-BaF_25	1409	1.10×10^{16}	1.04×10^{15}	-	-	-	34	-
Ap-BaF_26	1434	2.06×10^{16}	1.98×10^{15}	48 ± 6	22 ± 3	862 ± 137	64	114.9 ± 17.9
Ap-BaF_27	1638	1.73×10^{16}	2.03×10^{15}	(35 ± 7)	(14 ± 4)	(712 ± 193)	38	(138.4 ± 31.0)
Ap-BaF_28	1628	1.07×10^{16}	1.50×10^{15}	-	-	-	14	-

[a] For Ap-BaF, the alpha-stopping distance weighted parent nuclide concentrations (C_{aw}; see Section 2.5) listed were calculated based on the interpolated 5x5 µm parent nuclide maps (see Section 2.4). If the distance of the ^{4}He ablation spot to the grain boundary on the interpolated map is less than the maximum alpha-stopping distance for the specific element, C_{aw} is not calculated (e.g., Ap-BaF_4; see Section 2.5). Note that locating the ^{4}He spots on the parent nuclide map is subject to uncertainty, especially for non-straight grain boundaries. The undulating grain boundaries of Apatite-BaF are not accurately replicated on the interpolated map, leading to a discrepancy between the true grain boundary and the grain boundary as drawn in the interpolation. Thus, the C_{aw} calculation for spots close to the grain rim needs to be treated with caution. Where the interpolation adds area to the grain, C_{aw} values are reported in round brackets. Where the interpolated grain extent is smaller than the true grain, no C_{aw} is calculated, even though the ^{4}He spot's distance from the true grain boundary would permit it (e.g., Ap-BaF_1). We did not include affected spots for either case in the thermal modelling.

[b] c-axis orthogonal distance from the ^{4}He-measurement spot centre to the nearest grain rim.

[c] AHe is apatite (U-Th-Sm)/He.

SD is standard deviation.

3.2 In situ measured helium profiles

In the following, we describe the c-axis-perpendicular profiles used for thermal modelling. Data pertaining to the c-axis parallel profiles is not included here, as it does not provide any additional insights beyond what can be gained from comparing the c-axis-perpendicular profiles. The c-axis parallel data is available in the corresponding Zenodo repository (https://doi.org/10.5281/zenodo.15856623).

The ^{4}He concentration profiles measured perpendicular to the crystallographic c-axis in Apatite-URG and Apatite-BaF depict two distinct ^{4}He patterns (Fig. 2). The three ^{4}He profiles acquired in Apatite-URG are indistinguishable within measurement uncertainty and display an overall flat shape. Two of the three profiles (Ap-URG-P1 and Ap-URG-P2) may show a subtle trend of higher ^{4}He concentrations towards the grain rim (Fig. 2a). In contrast, the four Apatite-BaF ^{4}He profiles are concave-down with a significantly higher ^{4}He concentration near the grain centre and lower concentrations at the rims (Fig. 2b), a typical shape expected for slowly cooled grains (Shuster and Farley, 2004). The profiles are inconspicuous and agree within measurement uncertainty, except for Ap-BaF-P3, which displays significantly higher ^{4}He concentrations in one half of the grain compared to the other profiles. Notably, peak ^{4}He concentrations for Ap-BaF-P2, Ap-BaF-P3 and Ap-BaF-P4 were measured c. 30 µm off-centre. We did not analyse the profiles of Apatite-McClure due to high uncertainties in the ^{4}He measurements (Section 3.1), limiting their meaningfulness. The ^{4}He measurement details for Apatite-McClure are listed in Table B1.

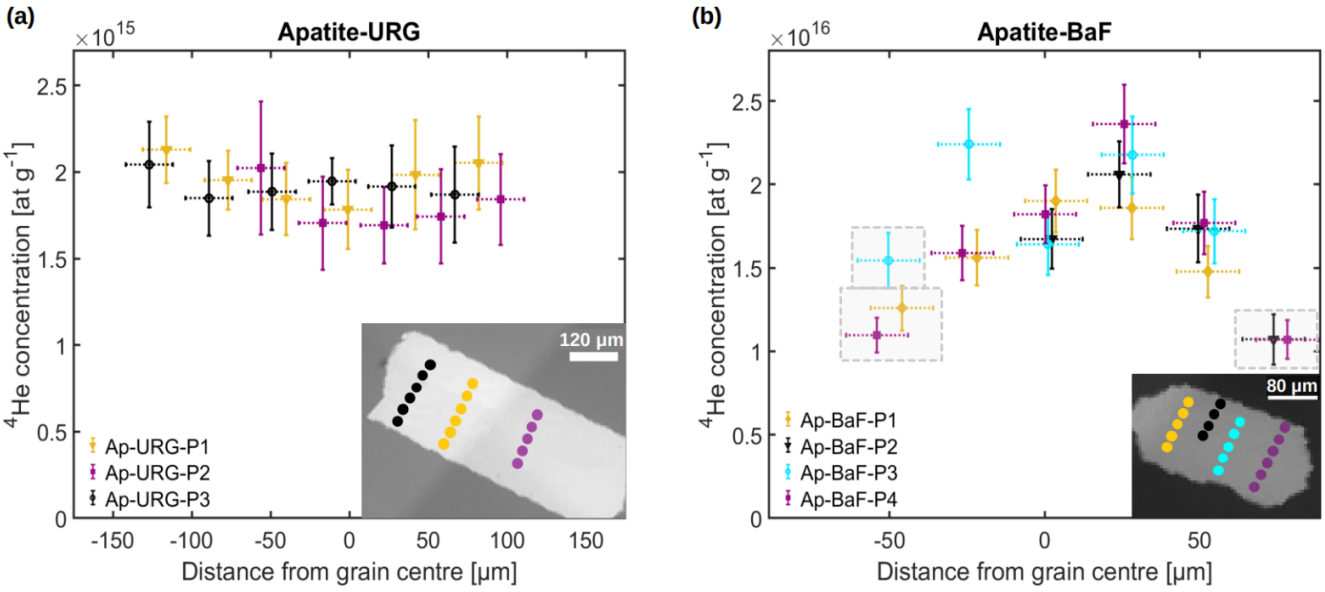

Figure 2: Measured in situ ^{4}He concentrations along c-axis-perpendicular rim-to-rim profiles in Apatite-URG (a) and Apatite-BaF (b). The coloured spots in the SEM images indicate the location of the corresponding ^{4}He measurements in each grain. The laser spot diameter was 30 µm for measurements in Apatite-URG and 20 µm for measurements in Apatite-BaF, indicated by the dashed horizontal error bars. Spots that are within 40 µm from the grain boundary are marked with grey boxes. These spots were excluded from inverse thermal history modelling (see Section 2.5).

3.3 Spatial variations in parent nuclide concentrations

Trace element mapping offers insight into the relationship between measured ^{4}He profiles and parent nuclide distribution. Figure 3 shows the uppermost U, Th, and Sm maps of Apatite-URG and Apatite-BaF, overlaid with alpha-stopping distance weighted parent nuclide concentrations C_{aw} for the ^{4}He ablation spots. Supplementary figure S3 presents the same for Apatite-McClure. In addition, Figure 4 displays all interpolated map slices of Apatite-BaF. Supplementary figures A1 and A2 show all map slices for Apatite-URG and Apatite-McClure.

Apatite-URG shows low ^{238}U concentrations (5–17 ppm), except for enriched grain rims and tips (Fig. 3a). ^{232}Th and ^{147}Sm span larger concentration ranges (86–234 ppm and 20–310 ppm, respectively) and variation compared to ^{238}U but do not show discernible zonation patterns in either map slice (Fig. 3b, c). For each element, C_{aw} does not deviate significantly from the concentrations seen in the uppermost parent nuclide map slice (Fig. 3a–c).

In contrast, Apatite-BaF has a heterogeneous parent nuclide distribution, with overall depth-consistent zonation in the ^{238}U (19–62 ppm), ^{232}Th (4–29 ppm), and ^{147}Sm (124–609 ppm) concentrations (Fig. 4). One side of the grain is enriched in parent nuclides compared to the other (Fig. 3e–h, Fig. 4). This matches the shapes of the measured ^{4}He concentration profiles that also display ^{4}He enrichment in one half of the grain compared to the other. While C_{aw} at each ^{4}He spot match the element distribution patterns of the uppermost map slice, ^{238}U C_{aw}, ^{232}Th C_{aw} and ^{147}Sm C_{aw} are overall slightly lower than in the uppermost map slice (Fig. 3e–g).

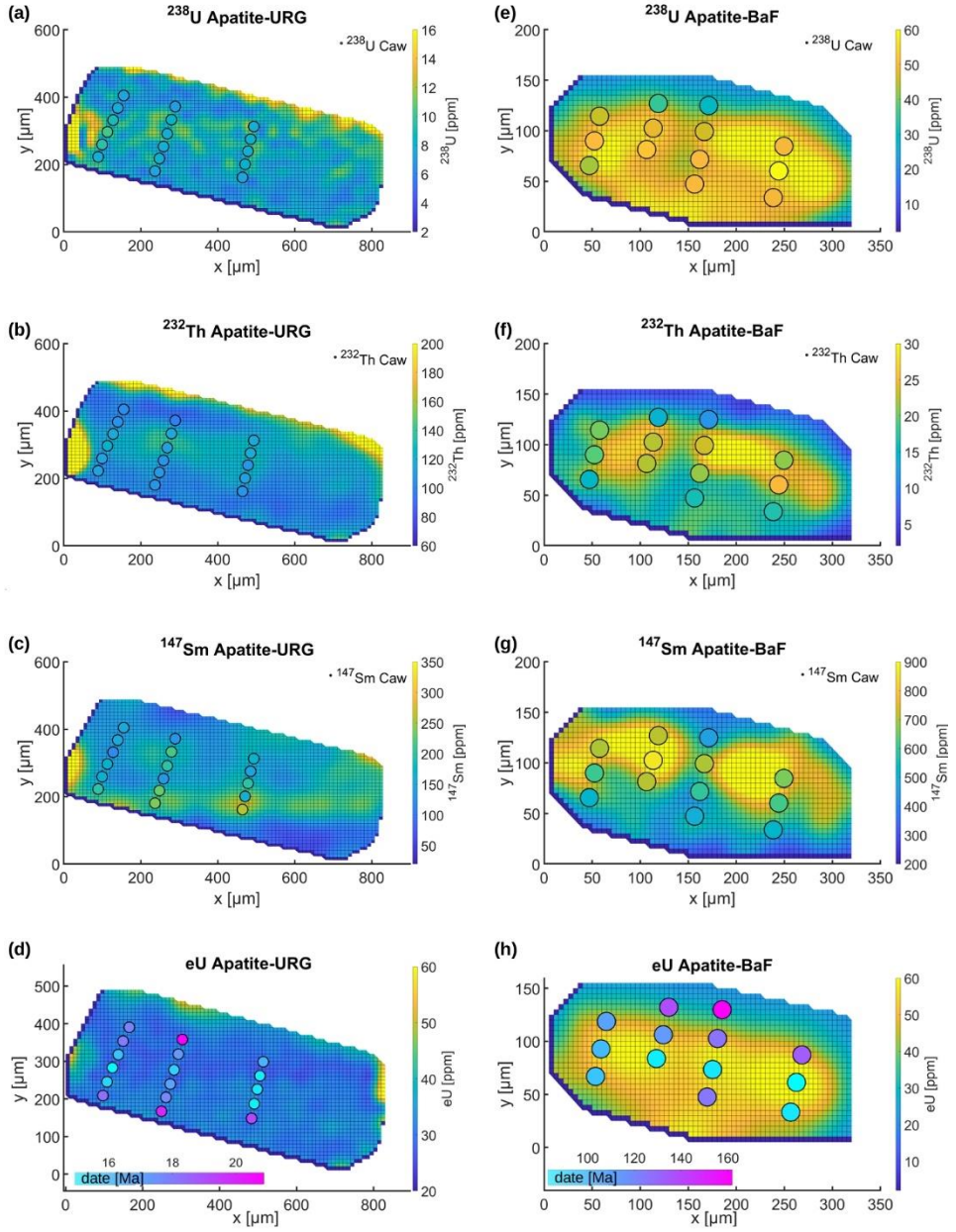

Figure 3: Interpolated parent nuclide (uppermost map slice) and eU maps (averaged over all slices) of the Apatite-URG (a–d) and Apatite-BaF (e–h) grains. The smoothness constraints (see Section 2.4) for Apatite-URG were λ=0.1 (U, Th) and 0.01 (Sm), and for Apatite-BaF λ=0.175 (U, Th) and λ=0.01 (Sm). Circles represent ablation spots for ^{4}He. Their size reflects the laser spot size, and colours reflect the calculated alpha-stopping-distance weighted parent nuclide concentration (C_{aw}) (upper three rows) and the calculated in situ date based on C_{aw} and ^{4}He concentration (d, h). Spots for which C_{aw} was not calculated (see Section 2.5) are not displayed.

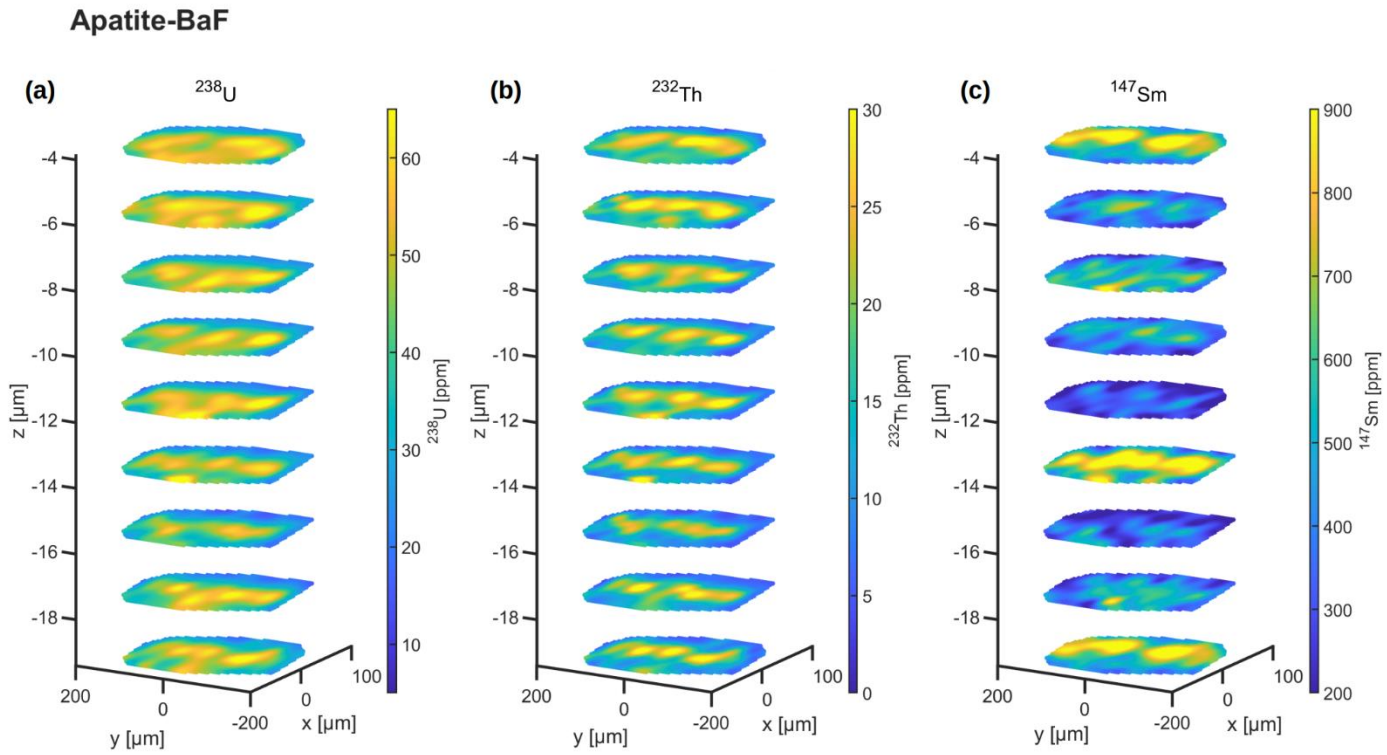

Figure 4: Interpolated parent nuclide distribution maps (5x5 µm horizontal resolution) of Apatite-BaF. Vertically, the parent nuclide concentrations were mapped approximately every 2 µm for a 20 µm deep section through the grain (parallel to the c-axis). The uppermost slice mapped at 2 µm depth is not displayed due to a large number of outlier measurements (Section 2.4). Parent nuclide maps were interpolated with a smoothness constraint (see Section 2.4) of λ=0.175 for the ^{238}U (a) and ^{232}Th (b) maps and λ=0.01 for the ^{147}Sm maps (c).

3.4 Spatial variation of in situ dates

In situ AHe dates are calculated from the ^{4}He concentration and C_{aw} and vary with the spot location in the grain (Fig. 3d, h). In Apatite-URG, the in situ dates are the same within error, ranging from 15.2 ± 2.5 Ma to 20.9 ± 3.1 Ma (1 SD). There is a trend of older in situ AHe dates closer to the grain rim, but a spatial correlation between the date pattern and eU is not evident (Fig. 3d). The weighted mean in situ AHe date of 17.2 ± 1.6 Ma is within the apatite U-Pb date of 16.75 ± 0.84 Ma, determined by Binder et al. (2023), for this sample.

The in situ AHe dates in Apatite-BaF show a larger range (83.2 ± 9.6 Ma to 162.3 ± 29.0 Ma, with a weighted mean date of 98.3 ± 41.8 Ma) and tend to be older towards the grain rims. Except for two anomalously old dates of spots closest to the grain boundary (Fig. 3h), in situ dates with a similar distance to the grain rim agree within measurement uncertainty. It appears that the youngest in situ dates are closest to the grain centre and in areas of the highest eU.

3.5 Cooling histories of two natural apatite crystals

3.5.1 Thermal histories from in situ helium profiles

In situ ^{4}He profiles and their corresponding C_{aw} can be inverted for cooling history reconstructions of single grains, which we tested for grains Apatite-URG (homogeneous) and Apatite-BaF (zoned).

We inverted the three ^{4}He profiles measured in Apatite-URG for time-temperature paths with the present-day mean annual temperature of 10 °C for Germany (German Weather Service DWD) as an endpoint constraint and allowing a deviation of ± 5 °C. The model starting point was 20 Ma and 550 °C based on the independently determined apatite U-Pb date of 16.75 ± 0.84 Ma (Binder et al., 2023). Due to the overlap in (U-Th-Sm)/He and U-Pb dates, we chose to widen the exploration space to 20 Ma instead of using the U-Pb age to avoid the starting point dictating the inversion results. Using these two constraints resulted in models with a large number of acceptable paths (i.e., GOF >5%) for all input ^{4}He profiles, but no good paths (i.e., GOF >50%) were retrieved (Fig. 5). Further, the ^{4}He profiles, forward-modelled based on the acceptable paths, align with the measured ^{4}He profiles within measurement uncertainty. The best-fitting cooling paths have misfits (Eq. 2, cf., Section 2.6) of m=1.37 (Ap-URG-P1), m=0.84 (Ap-URG-P2) and m=1.77 (Ap-URG-P3). All ^{4}He profile inversions and the corresponding best-fit forward models (Fig. 5a-c) indicate rapid cooling through the He PRZ between 15 and 20 Ma, which is both compatible with the volcanic nature of the sample (tuff) and the timing of magmatism inferred for the southern Upper Rhine Graben (Binder et al., 2023).

The in situ ^{4}He profile inversion for zoned Apatite-BaF only produced acceptable time-temperature paths for one of the four measured ^{4}He profiles (Ap-BaF-P1) (Fig. 6). Note that we only included ^{4}He spots for which C_{aw} could be calculated (Fig. 2, Table 3) in the inverse modelling. We used the same endpoint constraint for the time-temperature paths as for Apatite-URG, setting the temperature at 10 ± 5 °C for t=0 Ma. The starting point was set to a temperature of 570 °C at a time of 320 Ma, based on the weighted mean apatite U-Pb date derived from trace element measurements in Apatite-BaF (available in the associated Zenodo repository https://doi.org/10.5281/zenodo.15856623). Further, we used a study by Vamvaka et al. (2014) conducted near the sample location of Apatite-BaF in the Bavarian Forest (approximately 5–10 km from our sample location, same rock type), to assess the plausibility of our inversion results for Apatite-BaF. Based on their findings, we explored a cooling-only scenario (scenario 1) with the above start- and endpoint constraints (Fig. 6a, c) and an exhumation-and-reheating scenario (scenario 2, Fig. 6b, d). Specifically, Vamvaka et al. (2014) suggested possible reheating (re-burial) in the Bavarian Forest near the Apatite-BaF sample location during the Jurassic or Lower Cretaceous followed by exhumation in the Upper Cretaceous. To test whether this is plausible for our Apatite-BaF, we set model constraints for scenario 2 such that Jurassic and Cretaceous reburial is permitted but not required (Fig. 6b, d), with the additional limitation that temperatures in the Upper Cretaceous cannot exceed 120 °C (based on apatite fission track data by Vamvaka et al. (2014)). Moreover, we repeated both inversions with C_{aw} calculated from parent nuclide maps with different resolutions for sensitivity testing (cf., Section 3.5.2). The inversions for Ap-BaF-P1 resulted in a large number of acceptable time-temperature paths for both the cooling-only

scenario and the reburial-and-exhumation scenario. However, good paths were only resolved in the latter and when using C_{aw} calculated from a high-resolution parent nuclide map (Fig. 6d).

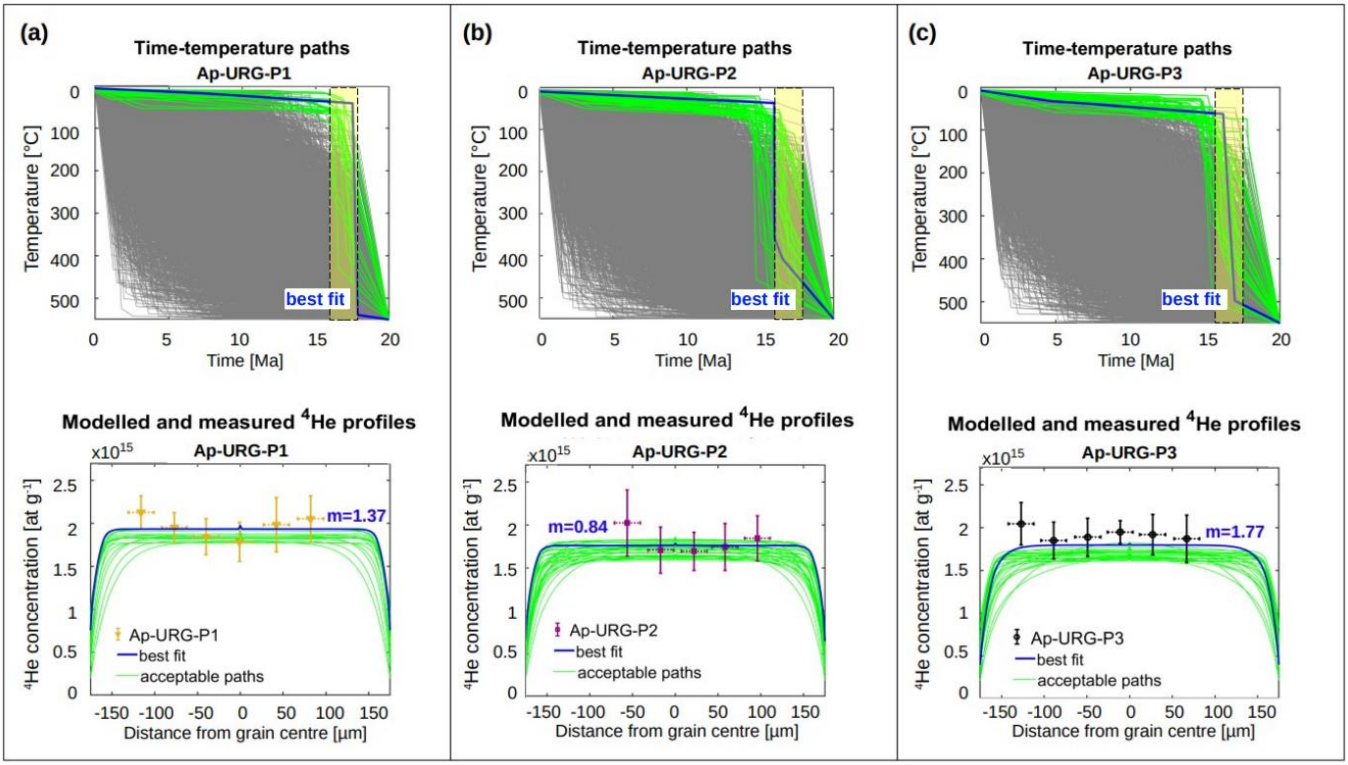

Figure 5: Cooling history reconstruction of grain Apatite-URG. The time-temperature (t-T) paths were retrieved by inverting the ^{4}He profile measurements (upper panels). Based on the acceptable t-T paths, the ^{4}He profiles were forward-modelled, assuming a homogeneous parent nuclide distribution (lower panels). The forward models combine two core-rim profiles, leading to a small jump in the modelled ^{4}He concentration in the centre of the grain (Section 2.6). Acceptable paths (in green) represent a GOF >5%. t-T paths and corresponding ^{4}He profiles with the lowest misfit m (Section 2.6, Eq.2) are highlighted in blue. The crystallisation date (apatite U-Pb date ± 1 standard deviation) of Apatite-URG as determined by Binder et al. (2023) is indicated by a yellow bar in the upper panels.

3.5.2 Sensitivity of the thermal models to parent nuclide map resolution

We repeated the inversion for Ap-BaF-P1 for the cooling-only (scenario 1) and for the reburial-and-exhumation scenario (scenario 2) twice to test the sensitivity of the inversion results to the parent nuclide map resolution. The first inversion used C_{aw} calculated from the initial 24x24-µm resolution parent nuclide map, while the second inversion utilised higher-resolution C_{aw} derived from the interpolated 5x5-µm resolution parent nuclide maps. As mentioned in Section 3.5.1, all four inversions produced acceptable paths. Notably, the misfit between the measured ^{4}He profile and the forward-modelled ^{4}He profile based on the best-fitting time-temperature path is lower for the models using 5x5-µm resolution C_{aw} (Fig. 6c, d) than for the models using 24x24-µm resolution C_{aw} (Fig. 6a, b) across both scenario 1 and scenario 2. Further, for the models using 24x24-µm resolution C_{aw} (Fig. 6a, b), the best-fit paths retrieved in scenario 1 and scenario 2 are very similar with misfits of m=2.42 (scenario 1, Fig. 6a) and m=2.45 (scenario 2, Fig. 6b). In contrast, when using the high-

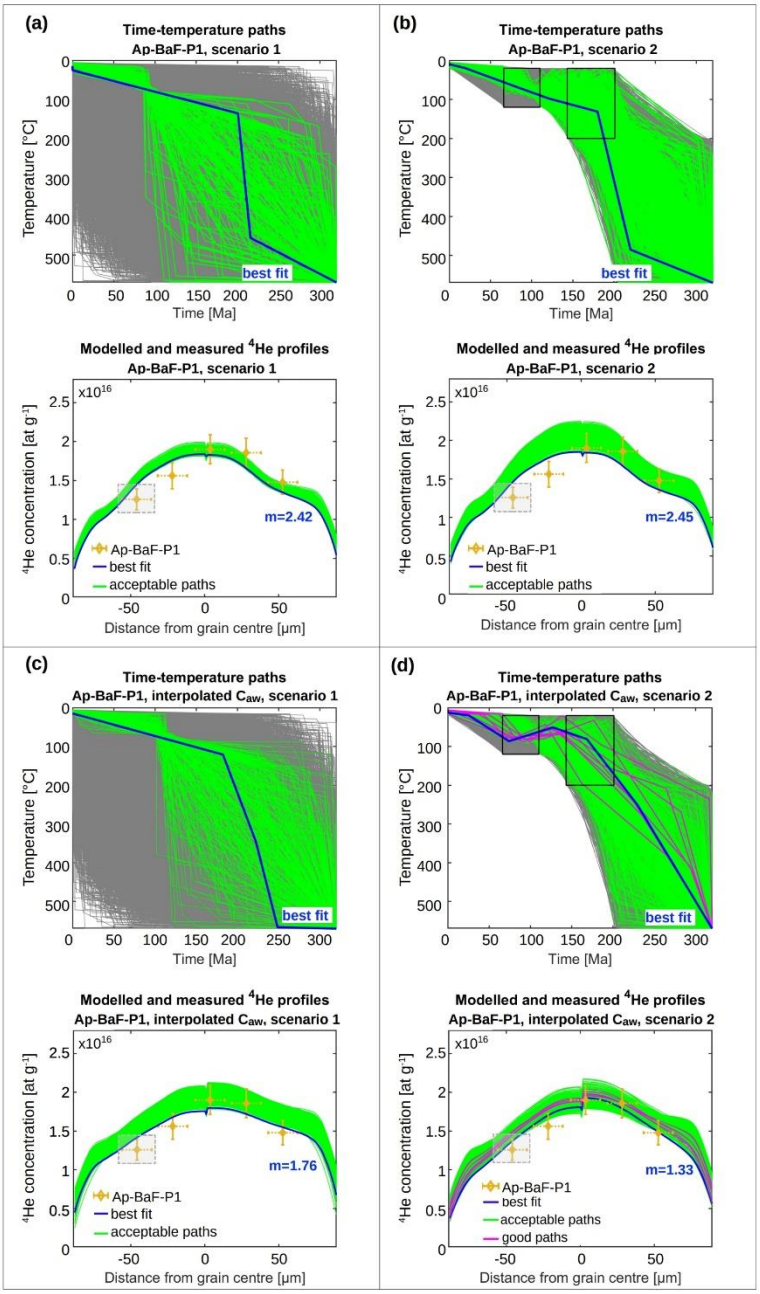

Figure 6: Cooling history reconstruction of grain Apatite-BaF testing a cooling-only scenario (scenario 1; a, c) and a reburial-and-exhumation scenario (scenario 2; b, d). The time-temperature (t-T) paths were retrieved by inverting the ^{4}He profile measurements and using alpha-stopping-distance weighted parent nuclide concentrations (C_{aw}) calculated based on the original 24x24-µm resolution measurements (a,b) and on the interpolated 5x5-µm resolution parent nuclide distributions (c,d). The different resolutions were used to assess the effect of parent nuclide map resolution on thermal modelling. Based on the acceptable t-T paths, the ^{4}He profiles were forward-modelled, assuming a heterogeneous parent nuclide distribution. The forward models combine two core-rim profiles, leading to a small jump in the modelled ^{4}He concentration in the centre of the grain (Section 2.6). Acceptable paths (in green) represent a GOF >5% and good paths (in magenta) represent a GOF >50%. t-T paths and corresponding ^{4}He profiles with the lowest misfit m (Section 2.6, Eq.2) are highlighted in blue. The black boxes indicate t-T constraints. Spots that are within 40 µm from the grain boundary are marked with grey boxes. These spots were excluded from inverse thermal history modelling but used for misfit calculation of the measured and forward-modelled ^{4}He profiles.

resolution C_{aw}, the misfit for the best-fit path in scenario 2 (with reheating, m=1.33, Fig. 6d) is distinctly lower than in scenario 1 (cooling only, m=1.76, Fig. 6c). Additionally, using high-resolution C_{aw}, the misfits for the best-fit paths are in the same range as for the homogeneous Apatite-URG.

3.6 Summary of the main results

The preceding paragraphs present the results of in situ ^{4}He profile measurements, parent nuclide mapping and thermal history modelling performed on two apatites from samples in South Germany (Apatite-URG and Apatite-BaF). We attained ^{4}He profiles with ^{4}He measurement uncertainties of less than 10% for Apatite-BaF (ablation spot diameter 20 µm) and less than 15% for Apatite-URG (ablation spot diameter 30 µm). Apatite-URG with a homogeneous parent nuclide distribution shows a redundancy between the three measured in situ ^{4}He profiles and in situ (U-Th-Sm)/He dates that are generally consistent within measurement uncertainty and overlap with the independently determined apatite U-Pb date of this sample (Binder et al., 2023). Thermal modelling for all ^{4}He profiles suggests that Apatite-URG underwent rapid cooling between 15 and 20 Ma.

In contrast, Apatite-BaF with a heterogeneous parent nuclide distribution displays a strong variation in in situ AHe dates from the core (younger) to the rim (older), with the youngest in situ dates corresponding to the areas of highest eU. Only one profile, Ap-BaF-P1, could be inverted to yield acceptable cooling paths. We tested a cooling-only scenario against a scenario of potential Jurassic or Lower Cretaceous reburial followed by Upper Cretaceous cooling as proposed by Vamvaka et al. (2014) for areas near Apatite-BaF's sample location. While the ^{4}He profile inversion for both scenarios yielded acceptable time-temperature paths, good paths were only achieved for the reburial-and-exhumation case, suggesting this to be the more fitting thermal history.

Sensitivity testing with C_{aw} calculated from different resolution parent nuclide maps indicates that inverse and forward models using C_{aw} calculated from high-resolution parent nuclide maps produce better results, i.e., a lower misfit between modelled and measured ^{4}He profiles, than models using C_{aw} from lower-resolution parent nuclide maps.

We make the following general observations that will be further discussed below. (1) There is a strong relation between ^{4}He measurement uncertainty and ablation spot size (volume), which needs to be selected to be large enough to reduce analytical uncertainty and small enough to increase spatial resolution. (2) In situ measured ^{4}He concentrations and corresponding in situ dates vary with the spot location in the grain and with eU. (3) In situ ^{4}He profiles can be inverted for cooling histories of homogeneous and, even though more challenging, heterogeneous grains.

4 Discussion

4.1 Grain size

The direct measurement of (in situ) ^{4}He profiles requires comparatively large grains, at least 145 µm in diameter in our case. There are two main controls on the minimum analysable grain size: the minimum number of spots needed for a reliable ^{4}He concentration profile (Section 4.2) and the minimum ablation spot diameter to reach the required ablation volume (Section

4.3). Regarding the former, our data suggest that at least four evenly spaced measurements (3–5 µm distance from rim to rim of the ablation spot) along a c-axis perpendicular half-profile (core to rim) or six along a rim-to-rim profile are necessary for a reliable ^{4}He concentration profile. With respect to the latter, we determined, for our laboratory set-up at the University of Tübingen, an ablation spot diameter of 20 µm as ideal for apatite (Section 4.3). Taken together, for a full profile of six spots with a spot size of 20 µm, a spot spacing of 5 µm and a zero distance between the edge of the outermost ablation spot and the grain rim, the minimum grain diameter is 145 µm. Grains with a low ^{4}He content ($<2.1\times10^{15}$ at g^{-1} in this study), requiring larger ablation spots, can only be analysed if a medium sand-sized fraction is available. This requirement limits the applicability of the single-grain in situ approach for thermal history modelling, especially for small apatites with low parent nuclide concentrations. In such cases where the grain size is small or the required spot size is large (or both), single in situ spots in several grains would have to be used (e.g., Glotzbach and Ehlers, 2024).

4.2 Number of ablation spots in a profile

The minimum number of ^{4}He spots needed for a profile measurement is crucial in assessing whether a grain is sufficiently large for in situ ^{4}He profile measurements. However, determining the minimum number of ablation spots in a profile is not trivial, as it depends on the complexity of the ^{4}He profile, which is unknown beforehand.

For a first estimate, we liken the minimum number of spots in a profile to the mathematical problem of finding the minimum number of unique points needed to define a curve. It is evident that two points define a straight line, and given any two distinct points, there is only one unique line fitting through them. The minimum number of points required to describe a curve, on the other hand, depends on its complexity. The simplest assumption is that if the definition of a straight line requires two points, a simple curve should require at least three. This assumption is valid for a simple quadratic function of the form $f(x) = ax^2 + bx + c$, representing a parabola. Thus, if we approximate the ^{4}He profile within a homogeneous grain as a parabola, then three points from the core to the rim, or six from rim to rim, are necessary to measure the ^{4}He profile. In the case of a parabolic ^{4}He profile that is symmetric about the c-axis (with the vertex of the parabola located at the centre of the grain), measuring five spots with the middle spot exactly at the grain centre may also be sufficient. We advise against using fewer spots in a rim-rim profile, as less than three measurements per grain half increases the risk of under-defining a core-rim section.

For the grains in this study, we achieved good results using five to six spots in a rim-rim profile and four in a core-rim profile. Thus, based on the mathematical thought experiment and our measurements, we conclude that starting with at least six spots in a rim-rim profile is appropriate. However, this is a minimum estimate, and we generally recommend using as many spots as possible to measure a ^{4}He profile for best results.

4.3 Laser ablation spot diameter and pit depth

The choice of ablation spot diameter and pit depth is a compromise between the accuracy of the ^{4}He concentration profile, which benefits from a smaller spot size and shallower pit, and the analytical uncertainty, which increases with decreasing ablated volume, i.e., decreasing amount of ^{4}He measured. Generally, the lower the difference between the ^{4}He signal and the

blank level, the higher the associated measurement uncertainty. This is illustrated by the measurements in Apatite-URG and Apatite-McClure. The uncertainty in the ^{4}He measurement for Apatite-McClure is more than four times greater than for Apatite-URG despite the similar ^{4}He concentrations. The reason for this significant difference lies in the ablation spot diameter. Measurements in Apatite-McClure had an ablation spot diameter of 10 µm, resulting in an ablated volume that is only about 7% of that in Apatite-URG, which had an ablation spot diameter of 30 µm. As a result, the ^{4}He signal for Apatite-McClure was too low to yield precise measurement results. The lower limit of the ablated volume depends on the ^{4}He concentration in the grain and the specific blank levels and criteria for acceptable analytical uncertainty of the analysing laboratory. In our laboratory, ^{4}He measurements are considered ideal when they exceed three times the standard deviation of our line blank measurements and have a standard deviation (SD) of <5%. While slightly lower ^{4}He signals are not ideal, they can still be used, with the caveat that their measurement uncertainties will increase when approaching blank levels. In this study, both Apatite-URG and Apatite-BaF have measurement uncertainties of >5%. We report the quality assessment for each measurement in the associated repository.

Another trade-off exists between smaller-diameter and deeper ablation pits and larger-diameter and shallower ablation pits. The uncertainty introduced by pit volume measurements is one of the limiting factors for the minimum ablation spot size. We determined pit volumes via confocal laser scanning microscopy, which is constrained by the maximum resolvable pit depth at small pit diameter-to-depth ratios. The difficulty with mapping the topography of increasingly narrow and deep pits is illustrated by the progressively higher standard deviations from the mean pit volume in our measurements at lower diameter-to-depth ratios (Table 2). Pickering et al. (2020) found the same type of limitations when using optical interferometry, which demonstrates the need for further development in determining pit volumes. An additional constraint on spot diameter vs. pit depth is a potential parent nuclide zonation. While a small-diameter but deep ablation pit reduces lateral averaging of the helium concentration, it exacerbates the effects of potential 'downhole' parent nuclide zonation and inclusions.

For this study, which includes 98 individual measurements with ablation spot sizes of 10–30 µm and corresponding average depths of 7.9 –9.7 µm (Table 2 and Table B1), a pit diameter of at least 20 µm and depth <8 µm was optimal. Likewise, Pickering et al. (2020) used 20 µm pit diameters with depths of <10 µm for their in situ AHe analysis. For zircons, Danišík et al. (2017) achieved reliable ^{4}He measurements for square spots with diameters of <10 µm and pit depths of ~2 µm. However, due to the above factors, we recommend that users conduct test measurements with different ablation pit geometries to determine what suits each sample best before measuring ^{4}He concentration profiles.

4.4 Laser ablation spot locations in the grain

The placement of ^{4}He ablation spots to measure an accurate in situ ^{4}He concentration profile for thermal history reconstruction mainly depends on two aspects: the distance to inclusions and fractures, and the distance of the outermost individual spots to the grain rim. Concerning the former, the distance to inclusions is critical, because mineral inclusions with a potentially many times higher parent nuclide concentration compared to the host crystal may implant foreign helium and lead to excess ^{4}He, not directly related to the cooling history, in the surrounding grain (e.g., Vermeesch et al., 2007). Furthermore, fractures or voids

can trap ^{4}He and locally affect the ^{4}He diffusion kinetics (e.g., Zeitler et al., 2017). As these phenomena complicate cooling history reconstructions, their periphery should be avoided. When selecting ^{4}He ablation spots, a minimum distance of 20 µm from inclusions or fractures (for average alpha-stopping distances, e.g., Pickering et al., 2020) should be maintained. Still, if possible, grains with these features should not be analysed. We discuss the effect of grain heterogeneities further in Section 4.6.

More crucial for ^{4}He profile measurements is the distance of a ^{4}He ablation spot to the grain rim, provided an adequate grain is selected. Close to the grain rim, ^{4}He measurements will average concentrations across a steep gradient (depending on the spot size) due to alpha-ejection at the grain boundary (e.g., Farley et al. 1996; Farley, 2002). This leads to a decreased accuracy of the measurements near the rim. To avoid grain rim effects and to account for the full range of alpha-stopping distances, an ablation spot would need to be at least 40 µm away from the grain boundary (distance from the ablation spot centre to the grain rim). However, this poses a problem since the shape of the helium profile near the grain rim is diagnostic for differentiation between slow and fast cooling. Ultimately, the difference between a flat (fast-cooled) ^{4}He profile and a rounded (slow-cooled) ^{4}He profile is best observed at the grain rim (Shuster and Farley, 2004). Not measuring ^{4}He within 40 µm of the grain rim would thus exclude characteristic information. In this exploratory study, we measured ^{4}He closer than 40 µm to the grain rim (Fig. 2) but did not calculate alpha-stopping distance weighted parent nuclide concentrations (C_{aw}) for those spots or use them for the ^{4}He profile inversion. Nevertheless, we included those measurements for comparisons between the measured and forward-modelled ^{4}He profiles. Further studies are needed to determine best practices concerning the ^{4}He spot placement and measurements near the grain rim.

Furthermore, our results for Apatite-URG (Fig. 2a) suggest that in homogeneous grains, the placement of the profile closer to the grain tips or middle does not influence the in situ ^{4}He profile's shape. Information gathered from multiple profiles in such cases is expected to be redundant, as demonstrated in all Ap-URG profiles (Fig. 2a) and in three of four Ap-BaF profiles that are indistinguishable within measurement error (Fig. 2b). Hence, for homogeneous or concentrically zoned grains, it may suffice to measure a half-profile. However, we still recommend analysing 2–3 rim-to-rim profiles because the likelihood of detecting anomalies in parent nuclide and ^{4}He distribution, e.g., due to inclusions, is higher.

4.5 Spatial variation of in situ dates in a grain

Apatite-BaF displays a strong variation of in situ AHe dates from core to rim, with a trend of older dates towards the grain rim and younger dates towards the grain centre (Fig. 3h). The pattern of older dates at the grain rim is the most pronounced in the profiles Ap-BaF-P2 and Ap-BaF-P3, where the dates at the rim are up to twice as old as the dates in the centre (Fig. 3h). Notably, profile Ap-BaF-P1, which we successfully inverted for thermal histories, does not show this trend.

The observed date distribution within Apatite-BaF is counterintuitive. In theory, uniform Arrhenius-type diffusion results in a relative depletion of ^{4}He at the rims compared to the core and a distribution of the oldest (U-Th-Sm)/He dates in the grain centre with progressively younger dates towards the grain rims (Glotzbach and Ehlers, 2024). A pattern of younger dates nearer to the rim would also be logical for a heterogeneous grain like Apatite-BaF, where the parent nuclides are relatively enriched

in the core compared to the rim (Fig. 3e-h). Here, the rims should be depleted in ^{4}He compared to the core, even when considering radiation damage effects (e.g., Shuster et al. 2006) and hence yield younger in situ dates. From our data, we cannot decipher the reason for the observed inverted in situ date pattern. It is unclear whether the oldest dates near the grain rims are outlier measurements or if they result from undetected local grain heterogeneities. Possible reasons for the old dates at the rim include a locally high alpha-particle production in the portion of the grain that was lost during the initial grinding and polishing after the grain was embedded in Teflon, or from deeper in the remaining unanalysed grain fraction. Additionally, there could be a higher local ^{4}He retentivity in the crystal lattice from variations in major element composition (e.g., Djimbi et al., 2015) or variations in vacancy damage (e.g., Gerin et al., 2017). Another factor to consider is an external source for high ^{4}He, such as the potential ^{4}He implantation from a neighbouring crystal. However, this is unlikely to have had an impact on the dates in Apatite-BaF as we only calculated in situ AHe dates for spots more than 40 µm from the grain rim, whereas the common assumption is that the outer 20 µm are the most affected by ^{4}He implantation (e.g., Spiegel et al., 2009; Gautheron et al., 2012). Moreover, Apatite-BaF does not show a ^{4}He concentration pattern indicative of ^{4}He implantation, which would be a significant peak in ^{4}He concentration at the grain rim facing the external ^{4}He source (cf., Gautheron et al., 2012). Thus, ^{4}He implantation is an unlikely reason for the date pattern in Apatite-BaF. Even so, the slightly older dates in Apatite-URG nearest to the grain rim in Ap-URG-P2 and Ap-URG-P3 (Fig. 3d), even though within measurement uncertainty, might be a result of ^{4}He implantation, as they do correspond with higher ^{4}He concentrations.

Regardless, in our modelling approach, we can only account for the redistribution of ^{4}He from the radioactive decay event via C_{aw} calculation. Any other processes that could locally deplete or enrich ^{4}He and lead to older in situ dates (e.g., lattice defects trapping ^{4}He) and alter the diffusive behaviour are not considered. Imaging techniques such as Raman spectroscopy would be necessary for further investigation and refinement.

4.6 Parent nuclide heterogeneity

Previous studies have evaluated the influence of parent nuclide zonation on ^{4}He profile thermal modelling in the context of whole grain ^{4}He/^{3}He analyses. They demonstrated that undetected and unquantified zonation of parent nuclides can result in retrieving incorrect cooling histories since parent nuclide heterogeneities do not always visibly manifest in the shape of the measured ^{4}He profile but still affect the ^{4}He concentration and distribution in the grain (e.g., Shuster and Farley, 2004; Farley et al., 2010). Hence, mapping the parent nuclide distribution of exposed internal grain surfaces is crucial in assessing the extent of parent nuclide heterogeneity influencing the ^{4}He distribution (e.g., Farley et al., 2011; Danišík et al., 2017).

In this study, Apatite-BaF exemplifies a case where the impact of parent nuclide zonation is not apparent from the measured ^{4}He profiles' shapes. The profiles Ap-BaF-P1, Ap-BaF-P2 and Ap-BaF-P4 (Fig. 2b) display an inconspicuous shape with a smooth decrease in ^{4}He concentration from the grain centre to the rim, typical for slowly cooled grains (Shuster and Farley, 2004), save for a slight skewing of the maximum concentration off-centre for Ap-BaF-P2 and Ap-BaF-P4. Even so, the comparison of measured and modelled ^{4}He profiles (Figs. 6a, b and 7) indicates that the ^{4}He gradient measured near the grain rim is not achievable solely by finding fitting time-temperature paths. The apparent discrepancy between measured and

modelled ^{4}He profiles near the grain rim, more so in the left side than the right (Fig. 6a, b, Fig.7), suggests a significant influence of parent nuclide heterogeneity (Figs. 2 and 3e–h) and associated variations in the ^{4}He production and diffusion in the crystal (e.g., Farley et al., 2010). This underlines that determining the parent nuclide distribution is a necessary step in interpreting in situ ^{4}He concentration profiles (e.g., Farley et al., 2011; Danišík et al., 2017; Fox et al., 2017).

4.7 Influence of parent nuclide map resolution on thermal modelling

Mapping the parent nuclide concentration on the exposed internal grain surface via LA-ICP-MS allows treating the in situ ^{4}He concentration as a function of the surrounding parent nuclide distribution to achieve more accurate ^{4}He profile-parent nuclide relationships for heterogeneous grains (e.g., Farley et al., 2010; Danišík et al., 2017). By using the alpha-stopping distance weighted parent nuclide concentration C_{aw} derived from such parent nuclide maps for ^{4}He profile thermal modelling, we can also account for the redistribution of ^{4}He from high-energy alpha decay (Section 2.5).

To illustrate the effect of parent nuclide heterogeneity on in situ ^{4}He profiles and as a first assessment of the thermal models' sensitivity to the parent nuclide map resolution, we compare forward-modelled ^{4}He profiles based on the same time-temperature path but assuming different parent nuclide distributions in Figure 7. As an example for a homogeneous grain, we compare the forward model results for Apatite-URG using a uniform parent nuclide distribution calculated as an average of all parent nuclide measurements (red curve, Fig. 7a), and using C_{aw} calculated from the 24x24-µm resolution parent nuclide map (blue curve, Fig. 7a). For the heterogeneous Apatite-BaF, we added a forward model using C_{aw} calculated from the higher-resolution, 5x5 µm, interpolated parent nuclide map (black line, Fig. 7b). We arbitrarily chose the best-fit time-temperature path retrieved by the respective inverse models in Figure 5a (Apatite-URG) and Figure 6c (Apatite-BaF) as a fixed input cooling history for the forward model tests. Figure 7a shows that for the mostly homogeneous Apatite-URG, the forward-modelled ^{4}He concentration profile using C_{aw} (blue curve, misfit=1.30; Fig. 7a) does not differ much from the forward-modelled ^{4}He profile based on an averaged, uniform parent nuclide distribution (red curve, misfit=1.37; Fig. 7a). The slight concave-up pattern of the measured ^{4}He profile (yellow data points, Fig. 7a), however, can solely be modelled with C_{aw}. Given that both models are indistinguishable within measurement uncertainty, we did not generate finer resolution models. In contrast, for the asymmetrically-zoned grain Apatite-BaF the shapes of the forward-modelled ^{4}He profiles differ significantly for the different parent nuclide distributions (Fig. 7b). Here, the forward-modelled ^{4}He profile based on the parent nuclide concentration measured closest to each in situ ^{4}He measurement location (red curve, m=4.19; Fig. 7b) is too steep and does not match the measured ^{4}He profile (yellow data points, Fig. 7b) towards the grain rim. The forward model with C_{aw} calculated from the measured 24x24-µm resolution parent nuclide map (blue curve, m=4.31; Fig. 7b) shows a comparable misfit. Although it captures the measured ^{4}He profile's shape, it overestimates the ^{4}He concentration in the left side of the grain. The smallest misfit between the measured and modelled 4He profiles is achieved when using C_{aw} from the interpolated 5x5-µm resolution parent nuclide maps (black curve, m=1.76; Fig. 7b). This is consistent with observations from the thermal modelling results shown in Figures 6, where the best results were achieved with the 5x5-µm resolution-based C_{aw} (Figs. 6c, d and Fig. 7).

In summary, while for homogeneous grains the difference in modelling results assuming a uniform parent nuclide distribution or C_{aw} is small, the parent nuclide distribution has a significant influence on the ^{4}He profile in heterogeneous grains. Further,

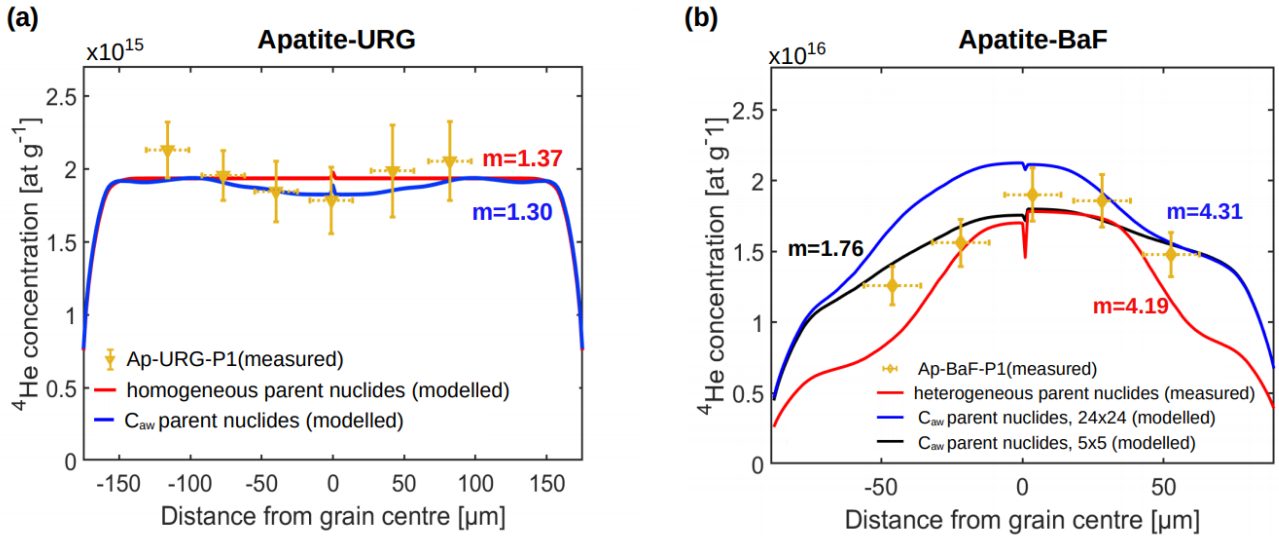

Figure 7: Influence of parent nuclide zonation on forward-modelled ^{4}He profiles. The profiles in (a) were forward-modelled based on the best-fit-path of profile Ap-URG-P1 (Fig. 5a), and the profiles in (b) were forward-modelled based on the best-fit path of Ap-BaF-P1 that resulted from the thermal history inversion in Figure 6c. The red curve in (a) is the forward-modelled ^{4}He profile assuming a grain-averaged homogeneous parent nuclide concentration, and the red curve in (b) is modelled using the parent nuclide concentration measured closest to each in situ ^{4}He measurement location in Ap-BaF-P1. The blue curves are forward-modelled ^{4}He profiles using the alpha-stopping distance weighted parent nuclide concentration C_{aw} calculated from the uninterpolated parent nuclide maps in both grains, and the black curve in (b) is the forward-modelled ^{4}He profile for Ap-BaF-P1 with C_{aw} based on the interpolated, higher resolution 5x5 µm element maps. m denotes the misfit between modelled and measured ^{4}He profiles (Section 2.6, Eq. 2). The forward models combine two core-rim profiles, leading to a small jump in the modelled ^{4}He concentration in the centre of the grain (Section 2.6).

it appears that models with C_{aw} from higher-resolution maps yield better results than models with C_{aw} from lower-resolution maps. However, evidence from one grain is limited and only a first step towards a systematic investigation into the optimal resolution for parent nuclide measurement and interpolation. Moreover, parent nuclide concentration interpolation and assumptions made in the calculation of C_{aw} (Section 2.5) introduce uncertainties, whose influence needs to be tested in future studies. To calculate C_{aw}, we assume that the grain's parent nuclide distributions are mirror-symmetric about the exposed internal surface due to half of the grain being lost during the grinding and polishing steps of sample preparation. Second, we assume that our determined ablation time-depth relationship holds (Section 2.4). Further uncertainty is introduced when localising the ^{4}He ablation spot centres on the LA-ICP-MS element maps, which is particularly critical for spots near the grain rim, where the interpolated grain boundary of the parent nuclide map does not always accurately capture the real grain boundary. Further studies are also required to test the optimal interpolation grid resolution in combination with the ablation spot size and the necessity of element maps of the entire grain. Regarding the latter, it might suffice to map the 40-µm proximity of the ^{4}He profile, covering the full alpha-stopping distance range. This would account for heterogeneities more efficiently, although information on potential element zonations of the entire grain surface would then not be available. This approach

could be augmented using other imaging techniques, such as cathodoluminescence, and Raman spectroscopy, to detect factors potentially affecting the ^{4}He diffusivity (e.g., Ault and Flowers, 2012; Danišík et al., 2017).

4.8 Cooling history reconstruction from single grains

We demonstrated through analyses of a homogenous apatite (Apatite-URG) and a heterogeneous apatite (Apatite-BaF) that the combination of situ ^{4}He measurements and C_{aw} calculated from element maps can be inverted for cooling histories of single grains. The example of Apatite-URG shows that the ^{4}He profile of a fast-cooled homogeneous grain as young as 16 Ma can be retrieved from six in situ spot measurements, and its cooling history can be accurately determined based thereon (Fig. 5). The example of Apatite-BaF shows that ^{4}He profiles of heterogeneous grains are more challenging to invert. Here, only one out of four ^{4}He profiles (Ap-BaF-P1, Fig. 2) could be successfully inverted for potential cooling histories. Even so, the inversion of Ap-BaF-P1 with high-resolution C_{aw} (Fig. 6d) resulted in a misfit between the forward-modelled and measured ^{4}He profiles comparable to results from the homogeneous Ap-URG. This suggests a potential for routine analysis of heterogeneous grains with the in situ method, pending further refinement. It is promising that although the profiles Ap-BaF-P2 to Ap-BaF-P4 could not be inverted for thermal histories, the acceptable cooling histories obtained from Ap-BaF-P1 align reasonably well with these profiles in forward models (Fig. C1, Appendix C).

One important development to be made in further studies is adjusting the modelling approach. Currently, the model is optimised for homogeneous grains, and a c-axis symmetric profile is assumed (Glotzbach and Ehlers, 2024). Apatite-BaF-P1 fulfils this symmetry assumption and thus could be inverted for cooling histories, while Apatite-BaF-P2 to Ap-BaF-P4 do not, and the inversion most likely fails for this reason.

While the forward models combine two core-rim profiles into a fully asymmetric rim-rim profile, we did not implement this approach in the inverse model; however, this could be a starting point for future studies. Additionally, further studies are needed to examine the effects of local changes in diffusivity mentioned in Section 4.5, such as the impact of radiation damage and whether this inhibits the modelling of heterogeneous grains.

4.9 Comparison with other single-grain thermal history reconstruction approaches

Our in situ ^{4}He profile approach is conceptually similar to the whole-grain ^{4}He/^{3}He method by Shuster and Farley (2004) and the in situ element-maps to 1D-profile method by Danišík et al. (2017). A key difference between the ^{4}He/^{3}He approach and the in situ methods is that the in situ approaches enable direct measurements of ^{4}He profiles. In contrast, the ^{4}He/^{3}He method requires proton irradiation of the samples to create a synthetic uniform ^{3}He distribution before helium measurement by step-wise degassing (cf., Shuster and Farley, 2004). This difference is crucial because the need for proton irradiation currently limits the accessibility of ^{4}He/^{3}He analyses (e.g., Colleps et al. 2024).

Danišík et al. (2017), who pioneered the concept of cooling history inversion from an in situ measured ^{4}He profile in zircon, illustrated that another advantage of in situ mapping of ^{4}He and parent nuclides compared to the whole-grain ^{4}He/^{3}He

measurement lies in the ability to analyse the spatial relationship between parent and daughter isotopes, as failing to account for the effect of grain heterogeneities on ^{4}He profiles can lead to inaccurate thermal models (Danišík et al., 2017).

Our approach differs from the protocol of Danišík et al. (2017) in that we do not perform ^{4}He and parent nuclide concentration mapping across the entire grain surface and convert those maps into 1D equivalent-sphere profiles. Instead, we directly obtain the ^{4}He profiles from spot measurements along c-axis-perpendicular transects through the grain and combine them with parent nuclide mapping. This method requires fewer individual ^{4}He analyses, improving efficiency. Furthermore, by integrating the ^{4}He profiles with C_{aw} from the element maps recorded at different "downhole" ablation depths, we can better understand the three-dimensional redistribution of ^{4}He and account for long alpha-stopping distances.

Even though further studies are needed to test the reliability of the in situ profile method, for example, by comparing results from different grains of the same sample, we suggest it provides a useful additional tool for cooling history reconstruction, especially for samples where grains of variable kinetics (i.e., grain sizes or eU) are not available to constrain possible time-temperature paths (for whole grain (U-Th-Sm)/He analyses) and where intracrystalline heterogeneities are prevalent.

5 Conclusion

In this exploratory study, we tested a new approach to obtain ^{4}He profiles in apatite from in situ measurements and model the cooling histories of single apatite grains. We examined the limitations regarding the location, size, and number of ablation spots, as well as the grain size needed to measure an interpretable in situ ^{4}He profile for our laboratory set-upat the University of Tübingen. Further, we introduced C_{aw}, an alpha-stopping distance weighted parent nuclide concentration at each ablation site, calculated from 2D trace element maps, to allow for thermal modelling from in situ ^{4}He measurements. We demonstrated the feasibility of our new approach on two natural apatite grains (one homogeneous, one zoned) from South Germany. From these results, we conclude the following:

1. The measurement of reliable ^{4}He profiles using the in situ (U-Th-Sm)/He approach is limited by minimum requirements on grain size and ablated volume. For our laboratory set-up in Tübingen, we find apatites that are larger than 145 µm and have with ^{4}He concentrations greater than 1×10^{16} at g^{-1} are most suitable to achieve satisfactory results. These dimensions may vary among different laboratories.
2. Our data indicate that obtaining a ^{4}He concentration profile requires at least four measurements from the grain core to the rim or six from rim to rim.
3. LA-ICP-MS parent nuclide mapping helps detect intracrystalline heterogeneities. The calculation of C_{aw} is crucial in analysing heterogeneous grains, but may be unnecessary in homogeneous grains where the benefit of C_{aw} calculations compared to using an averaged homogeneous parent nuclide concentration is marginal. This is important since parent nuclide mapping, inversion for 2D maps, and C_{aw} calculation can be time-consuming. To improve efficiency, one possibility is to map the 40 µm perimeter surrounding the ^{4}He spots for parent nuclides instead of the entire grain surface. This approach would suffice for the calculation of C_{aw}. However, it limits the

information available on grain zonation patterns and crystal lattice heterogeneities, which could be vital for interpreting asymmetric ^{4}He profiles. Therefore, the trade-off between efficiency and potential information loss needs to be systematically tested.

4. Cooling histories can be inverted from in situ ^{4}He profiles and parent nuclide maps. While the method is readily applicable to homogeneous grains, the inversion of asymmetric ^{4}He profiles (heterogeneous grains) would benefit from further studies and is thus not yet recommended for routine analysis.

Code and data availability

The code to calculate C_{aw}, along with a test file, and supplementary data including all grain photomicrographs, He measurement details, and all U, Th, and Sm measurements, can be found here: https://doi.org/10.5281/zenodo.15856623.

Author contributions

AKM: data curation, formal analysis, investigation, methodology, software, visualisation, writing – original draft; CG: conceptualisation, methodology, funding acquisition, resources, software, supervision, validation, writing – review & editing; SF: supervision, writing – review & editing.

Competing interests

The authors declare that they have no conflict of interest.

Acknowledgements

We thank Dominic Raisch from the Petrology and Mineral Resources Research Group at the University of Tübingen for SEM imaging. This study was supported by a grant from the Bundesgesellschaft für Endlagerung to Christoph Glotzbach (BGE – STAFuE-21-12-Klei), and funding for large equipment from the DFG (INST 37/1041-1 and 37/1207-1 FUGG).
We thank Olga Yakubovich and Julien Amalberti for their detailed and constructive reviews, and Cécile Gautheron for editorial handling.

References

Alexander E., Mickelson G. and Lanphere M.: MMhb-1: a new 40Ar-39Ar dating standard, Short Papers of the Fourth International Conference, Geochronology, Cosmochronology, and Isotope Geology. U.S. Geological Survey., 78–701, 6–8, 1978.

Anderson, A. J., Hodges, K. V., and van Soest, M. C.: Empirical constraints on the effects of radiation damage on helium diffusion in zircon, Geochimica et Cosmochimica Acta, 218, 308–322, https://doi.org/10.1016/j.gca.2017.09.006, 2017.

Ault, A. K., and Flowers, R. M.: Is apatite U-Th zonation information necessary for accurate interpretation of apatite (U-Th)/He thermochronometry data?, Geochimica et Cosmochimica Acta, 79, 60–78, https://doi.org/10.1016/j.gca.2011.11.037, 2012.

Ault, A. K., Gautheron, C., and King, G. E.: Innovations in (U–Th)/He, Fission Track, and Trapped Charge Thermochronometry with Applications to Earthquakes, Weathering, Surface-Mantle Connections, and the Growth and Decay of Mountains, Tectonics, 38(11), 3705–3739, https://doi.org/10.1029/2018TC005312, 2019.

Beucher, R., Brown, R. W., Roper, S., Stuart, F., and Persano, C.: Natural age dispersion arising from the analysis of broken crystals: Part II. Practical application to apatite (U-Th)/He thermochronometry, Geochimica et Cosmochimica Acta, 120, 395–416, https://doi.org/10.1016/j.gca.2013.05.042, 2013.

Binder, T., Marks, M. A. W., Gerdes, A., Walter, B. F., Grimmer, J., Beranoaguirre, A., Wenzel, T., and Markl, G.: Two distinct age groups of melilitites, foidites, and basanites from the southern Central European Volcanic Province reflect lithospheric heterogeneity, International Journal of Earth Sciences, 112(3), 881–905, https://doi.org/10.1007/s00531-022-02278-y, 2023.

Boyce, J. W., Hodges, K. V., Olszewski, W. J., Jercinovic, M. J., Carpenter, B. D., and Reiners, P. W.: Laser microprobe (U-Th)/He geochronology, Geochimica et Cosmochimica Acta, 70(12), 3031–3039, https://doi.org/10.1016/j.gca.2006.03.019, 2006.

Brown, R. W., Beucher, R., Roper, S., Persano, C., Stuart, F., and Fitzgerald, P.: Natural age dispersion arising from the analysis of broken crystals. Part I: Theoretical basis and implications for the apatite (U-Th)/He Thermochronometer, Geochimica et Cosmochimica Acta, 122(120), 478–497, https://doi.org/10.1016/j.gca.2013.05.041, 2013.

Colleps, C. L., van der Beek, P. A., Amalberti, J., Denker, A., Tremblay, M. M., Bernard, M., Dittwald, A. H., & Bundesmann, J.: Improving the Accessibility and Efficiency of Proton Irradiations for 4He/3He Thermochronology, Geochemistry, Geophysics, Geosystems, 25(2), https://doi.org/10.1029/2023GC011334, 2024

Danišík, M., McInnes, B. I. A., Kirkland, C. L., McDonald, B. J., Evans, N. J., and Becker, T.: Seeing is believing: Visualization of He distribution in zircon and implications for thermal history reconstruction on single crystals, Science Advances, 3(2), 1–10, https://doi.org/10.1126/sciadv.1601121, 2017.

Djimbi, D. M., Gautheron, C., Roques, J., Tassan-Got, L., Gerin, C., & Simoni, E.: Impact of apatite chemical composition on (U-Th)/He thermochronometry: An atomistic point of view, Geochimica et Cosmochimica Acta, 167, 162–176, https://doi.org/10.1016/j.gca.2015.06.017, 2015.Ehlers, T. A.: Crustal Thermal Processes and the Interpretation of Thermochronometer Data, Reviews in Mineralogy and Geochemistry; 58(1), 315–350, https://doi.org/10.2138/rmg.2005.58.12, 2005.

Farley, K. A., Wolf, R. A., and Silver, L. T.: The effects of long alpha-stopping distances on (U-Th)/He ages, Geochimica et Cosmochimica Acta, 60(21), 4223–4229, https://doi.org/10.1016/S0016-7037(96)00193-7, 1996.

Farley, K. A.: (U-Th)/ He Dating: Techniques, Calibrations, and Applications, Mineralogy and Geochemistry, 47(1), 819–844, https://doi.org/10.2138/rmg.2002.47.18, 2002.

Farley, K. A., Shuster, D. L., Watson, E. B., Wanser, K. H., and Balco, G.: Numerical investigations of apatite 4He/3He thermochronometry, Geochemistry, Geophysics, Geosystems, 11(10), 1–18, https://doi.org/10.1029/2010GC003243, 2010.

Farley, K. A., Shuster, D. L., and Ketcham, R. A.: U and Th zonation in apatite observed by laser ablation ICPMS, and implications for the (U-Th)/He system, Geochimica et Cosmochimica Acta, 75(16), 4515–4530, https://doi.org/10.1016/j.gca.2011.05.020, 2011.

Fitzgerald, P. G., Baldwin, S. L., Webb, L. E., and O'Sullivan, P. B.: Interpretation of (U-Th)/He single grain ages from slowly cooled crustal terranes: A case study from the Transantarctic Mountains of southern Victoria Land, Chemical Geology, 225(1–2), 91–120, https://doi.org/10.1016/j.chemgeo.2005.09.001, 2006.

Flowers, R. M.: Exploiting radiation damage control on apatite (U-Th)/He dates in cratonic regions, Earth and Planetary Science Letters, 277(1–2), 148–155, https://doi.org/10.1016/j.epsl.2008.10.005, 2009.

Flowers, R. M., Ketcham, R. A., Shuster, D. L., and Farley, K. A.: Apatite (U-Th)/He thermochronometry using a radiation damage accumulation and annealing model, Geochimica et Cosmochimica Acta, 73(8), 2347–2365, https://doi.org/10.1016/j.gca.2009.01.015, 2009.

Flowers, R. M., and Kelley, S. A.: Interpreting data dispersion and "inverted" dates in apatite (U-Th)/He and fission-track datasets: An example from the US midcontinent, Geochimica et Cosmochimica Acta, 75(18), 5169–5186, https://doi.org/10.1016/j.gca.2011.06.016, 2011.

Fox, M., Tripathy-Lang, A., and Shuster, D. L.: Improved spatial resolution of elemental maps through inversion of LA-ICP-MS data, Chemical Geology, 467(1), 30–4, https://doi.org/10.1016/j.chemgeo.2017.07.001, 2017.

Gautheron, C., Tassan-Got, L., Ketcham, R. A., and Dobson, K. J.: Accounting for long alpha-particle stopping distances in (U–Th–Sm)/He geochronology: 3D modeling of diffusion, zoning, implantation, and abrasion, Geochimica et Cosmochimica Acta, 96, 44–56, https://doi.org/10.1016/j.gca.2012.08.016, 2012.

Gautheron, C., Pinna-Jamme, R., Derycke, A., Ahadi, F., Sanchez, C., Haurine, F., Monvoisin, G., Barbosa, D., Delpech, G., Maltese, J., Sarda, P., and Tassan-Got, L.: Technical note: Analytical protocols and performance for apatite and zircon (U–Th)/He analysis on quadrupole and magnetic sector mass spectrometer systems between 2007 and 2020, Geochronology, 3, 351–370, https://doi.org/10.5194/gchron-3-351-2021, 2021.

Gerin, C., Gautheron, C., Oliviero, E., Bachelet, C., Mbongo Djimbi, D., Seydoux-Guillaume, A. M., Tassan-Got, L., Sarda, P., Roques, J., & Garrido, F.: Influence of vacancy damage on He diffusion in apatite, investigated at atomic to mineralogical scales, Geochimica et Cosmochimica Acta, 197, 87–103, https://doi.org/10.1016/j.gca.2016.10.018, 2017.

Glotzbach, C., Lang, K. A., Avdievitch, N. N., and Ehlers, T. A.: Increasing the accuracy of (U-Th(Sm))/He dating with 3D grain modelling, Chemical Geology, 506, 113–125, https://doi.org/10.1016/j.chemgeo.2018.12.032, 2019.

Glotzbach, C. and Ehlers, T. A.: Interpreting cooling dates and histories from laser ablation in situ (U–Th–Sm)/He thermochronometry: a modelling perspective, Geochronology, 6, 697–717, https://doi.org/10.5194/gchron-6-697-2024, 2024.

Guenthner, W. R., Reiners, P. W., Ketcham, R. A., Nasdala, L., and Giester, G.: Helium diffusion in natural zircon: radiation damage, anisotropy, and the interpretation of zircon (U-TH)/He thermochronology, American Journal of Science, 313(3), 145–198, https://doi.org/10.2475/03.2013.01, 2013.

Hansen, P. C., and O'Leary, D. P.: The Use of the L-Curve in the Regularization of Discrete Ill-Posed Problems, SIAM Journal on Scientific Computing, 14(6), 1487–1503, https://doi.org/10.1137/0914086, 1993.

Horne, A. M., van Soest, M. C., Hodges, K. V., Tripathy-Lang, A., and Hourigan, J. K.: Integrated single crystal laser ablation U/Pb and (U-Th)/He dating of detrital accessory minerals - Proof-of concept studies of titanites and zircons from the Fish Canyon tuff, Geochimica et Cosmochimica Acta, 178, 106–123. https://doi.org/10.1016/j.gca.2015.11.044, 2016.

Idleman, B. D., Zeitler, P. K., and McDannell, K. T.: Characterization of helium release from apatite by continuous ramped heating, Chemical Geology, 476, 223–232, https://doi.org/10.1016/j.chemgeo.2017.11.019, 2018.

Ketcham, R. A.: Forward and inverse modeling of low-temperature thermochronometry data, Reviews in Mineralogy and Geochemistry, 58, 275–314. https://doi.org/10.2138/rmg.2005.58.11, 2005.

Ketcham, R. A., Gautheron, C., & Tassan-Got, L.: Accounting for long alpha-particle stopping distances in (U-Th-Sm)/He geochronology: Refinement of the baseline case, Geochimica et Cosmochimica Acta, 75(24), 7779–7791. https://doi.org/10.1016/j.gca.2011.10.011, 2011.

Ketcham, R.A., Mora, A. and Parra, M.: Deciphering exhumation and burial history with multi-sample down-well thermochronometric inverse modelling, Basin Research, 30, 48-64, https://doi.org/10.1111/bre.12207, 2018.

Ketcham, R. A.: Thermal history inversion from thermochronometric data and complementary information: New methods and recommended practices, Chemical Geology, 653, 122042. https://doi.org/10.1016/j.chemgeo.2024.122042, 2024.

McDowell, F. W., Mcintosh, W. C., and Farley, K. A.: A precise 40 Ar – 39 Ar reference age for the Durango apatite (U–Th)/He and fission-track dating standard, 214, 249–263, https://doi.org/10.1016/j.chemgeo.2004.10.002, 2005.

McInnes, B. I. A., Evans, N. J., Fu, F. Q., and Garwin, S.: Application of thermochronology to hydrothermal ore deposits, Reviews in Mineralogy and Geochemistry, 58, 467–498, https://doi.org/10.2138/rmg.2005.58.18, 2005.

Paton, C., Woodhead, J. D., Hellstrom, J. C., Hergt, J. M., Greig, A., and Maas, R.: Improved laser ablation U-Pb zircon geochronology through robust downhole fractionation correction, Geochemistry, Geophysics, Geosystems, 11(3), Q0AA06, https://doi.org/10.1029/2009GC002618, 2010.

Pickering, J., Matthews, W., Enkelmann, E., Guest, B., Sykes, C., and Koblinger, B. M.: Laser ablation (U-Th-Sm)/He dating of detrital apatite, Chemical Geology, 548, 119683, https://doi.org/10.1016/j.chemgeo.2020.119683, 2020.

Reiners, P. W., and Farley, K. A.: Influence of crystal size on apatite (U-Th)/He thermochronology: An example from the Bighorn Mountains, Wyoming, Earth and Planetary Science Letters, 188(3–4), 413–420, https://doi.org/10.1016/S0012-821X(01)00341-7, 2001.

Reiners, P. W., Thomson, S. N., Mcphillips, D., Donelick, R. A., & Roering, J. J.: Wildfire thermochronology and the fate and transport of apatite in hillslope and fluvial environments, 112, https://doi.org/10.1029/2007JF000759, 2007.Schoene, B., and Bowring, S. A.: U-Pb systematics of the McClure Mountain syenite: Thermochronological constraints on the age of the 40Ar/39Ar standard MMhb, Contributions to Mineralogy and Petrology, 151(5), 615–630, https://doi.org/10.1007/s00410-006-0077-4, 2006.

Shuster, D. L., and Farley, K. A.: 4He/3He thermochronometry, Earth and Planetary Science Letters, 217(1–2), 1–17, https://doi.org/10.1016/S0012-821X(03)00595-8, 2004.

Shuster, D. L., Flowers, R. M., and Farley, K. A.: The influence of natural radiation damage on helium diffusion kinetics in apatite, Earth and Planetary Science Letters, 249(3–4), 148–161, https://doi.org/10.1016/j.epsl.2006.07.028, 2006.

Sousa, F. J., Cox, S. E., Rasbury, E. T., Hemming, S. R., Lanzirotti, A., and Newville, M.: U and Th zonation in apatite observed by synchrotron X-ray fluorescence tomography and implications for the (U–Th)/He system, Geochronology, 6, 553–570, https://doi.org/10.5194/gchron-6-553-2024, 2024.

Spiegel, C., Kohn, B., Belton, D., Berner, Z., and Gleadow, A.: Apatite (U-Th-Sm)/He thermochronology of rapidly cooled samples: The effect of He implantation, Earth and Planetary Science Letters, *285*(1–2), 105–114, https://doi.org/10.1016/j.epsl.2009.05.045, 2009.

Vamvaka, A., Siebel, W., Chen, F., and Rohrmüller, J.: Apatite fission-track dating and low temperature history of the Bavarian Forest (southern Bohemian Massif), International Journal of Earth Sciences, 103(1), 103–119, https://doi.org/10.1007/s00531-013-0945-x, 2014.

Vermeesch, P., Seward, D., Latkoczy, C., Wipf, M., Günther, D., and Baur, H.: α-Emitting mineral inclusions in apatite, their effect on (U-Th)/He ages, and how to reduce it, Geochimica et Cosmochimica Acta, 71(7), 1737–1746, https://doi.org/10.1016/j.gca.2006.09.020, 2007.

Vermeesch, P., Sherlock, S. C., Roberts, N. M. W., and Carter, A.: A simple method for in-situ U-Th-He dating, Geochimica et Cosmochimica Acta, *79*, 140–147. https://doi.org/10.1016/j.gca.2011.11.042, 2012.

Vermeesch, P., Tian, Y., Schwanethal, J., and Buret, Y.: Technical note: In situ U–Th–He dating by $^{4}He/^{3}He$ laser microprobe analysis, Geochronology, 5, 323–332, https://doi.org/10.5194/gchron-5-323-2023, 2023.

Wolf, R. A., Farley, K. A., & Silver, L. T.: Helium diffusion and low-temperature thermochronometry of apatite, Geochimica et Cosmochimica Acta, 60(21), 4231–4240, https://doi.org/10.1016/S0016-7037(96)00192-5, 1996.

Wolf, R. A., Farley, K. A., & Kass, D. M.: Modeling of the temperature sensitivity of the apatite (U-Th)/He thermochronometer. Chemical Geology, 148(1–2), 105–114, https://doi.org/10.1016/S0009-2541(98)00024-2, 1998.

Zeitler, P. K., Herczeg, A. L., McDougall, I., and Honda, M.: U-Th-He dating of apatite: A potential Thermochronometer, Geochimica et Cosmochimica Acta, 51(10), 2865–2868, https://doi.org/10.1016/0016-7037(87)90164-5, 1987.

Zeitler, P. K., Enkelmann, E., Thomas, J. B., Watson, E. B., Ancuta, L. D., & Idleman, B. D.: Solubility and trapping of helium in apatite, Geochimica et Cosmochimica Acta, 209, 1-8. https://doi.org/10.1016/j.gca.2017.03.041, 2017

Appendix A: Additional interpolated parent nuclide maps of Apatite-URG and Apatite-McClure

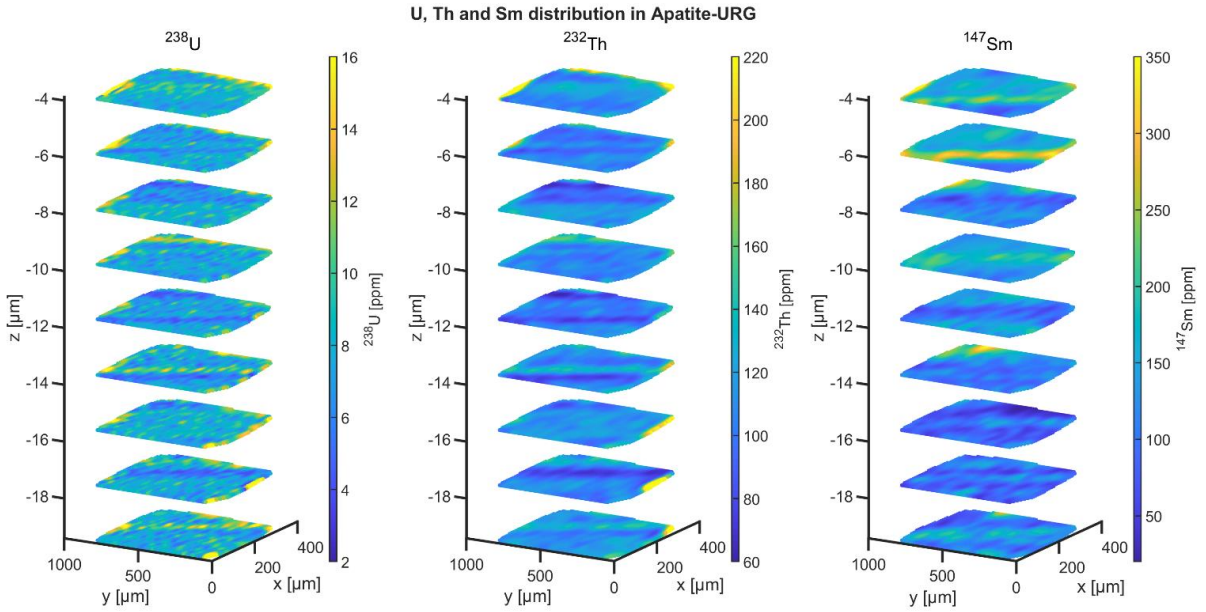

Figure A1: Interpolated parent nuclide distribution maps (10x10 µm horizontal resolution) of Apatite-URG. Vertically, the parent nuclide concentrations were recorded approximately every 2 µm for a 20 µm deep section in the grain. Parent nuclide maps were interpolated with a smoothness constraint of λ=0.1 for the ^{238}U and ^{232}Th and λ=0.01 for the ^{147}Sm maps.

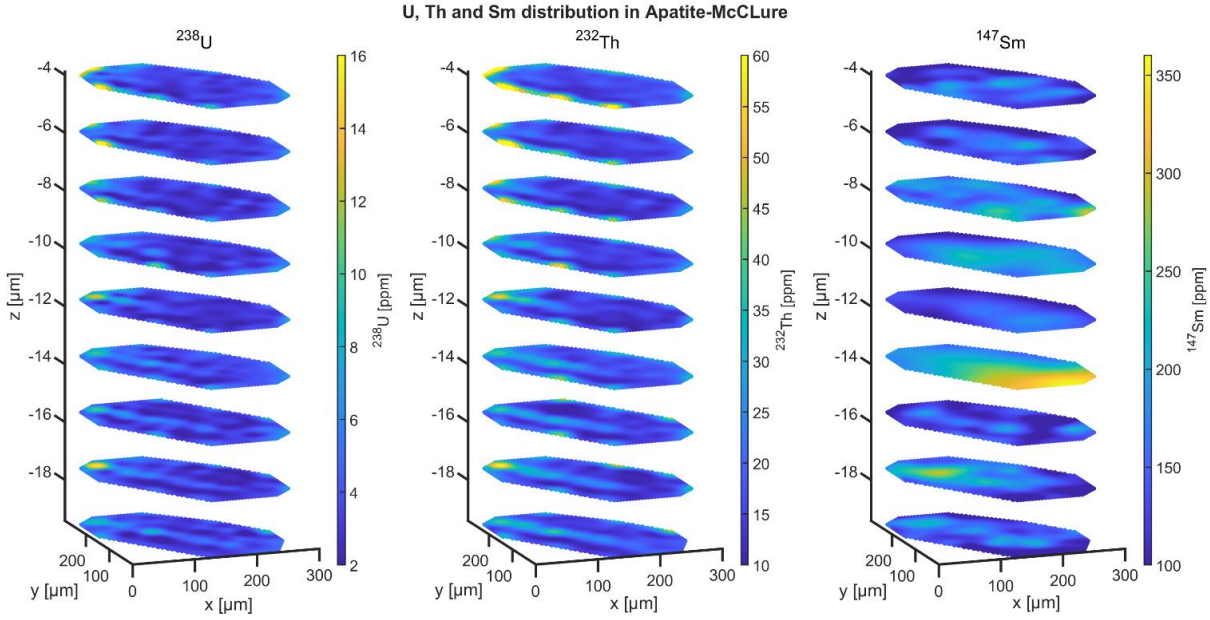

Figure A2: Interpolated parent nuclide distribution maps (5x5 µm horizontal resolution) of Apatite-McClure. Vertically, the parent nuclide concentrations were recorded approximately every 2 µm for a 20 µm deep section in the grain. Parent nuclide maps were interpolated with a smoothness constraint of λ=0.3 for the ^{238}U and ^{232}Th and λ=0.01 for the ^{147}Sm maps.

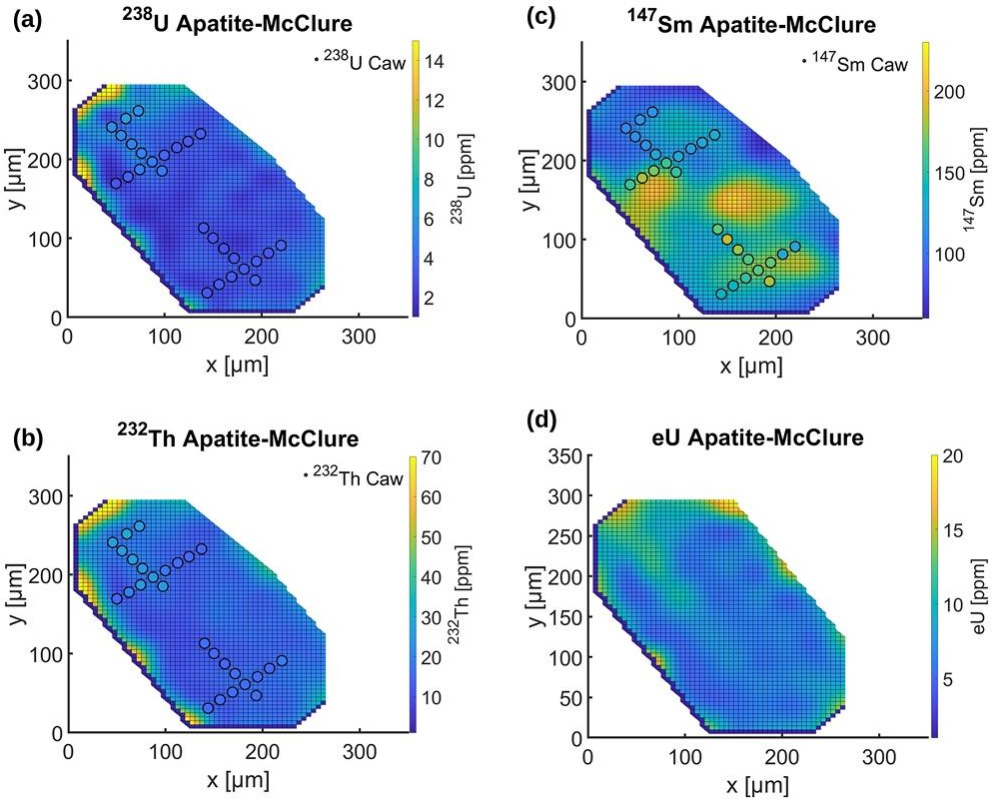

Figure A3: Interpolated parent nuclide (uppermost map slice) and eU maps (averaged over all slices) of Apatite-McClure. The smoothness constraints (see Section 2.4) were λ=0.3 (U, Th) and 0.1 (Sm). Circles represent ablation spots for ^{4}He. Their size reflects the laser spot size, and colours reflect the calculated alpha-stopping-distance weighted parent nuclide concentration (C_{aw}).

Appendix B: Apatite in situ ^{4}He measurements

Table B1: Apatite-McClure ^{4}He data and alpha-stopping distance weighted parent nuclides concentrations (C_{aw})

Spot	Pit volume [µm^3]	^{4}He [at g^{-1}]	^{4}He SD [at g^{-1}]	^{238}U C_{aw} ± 1SD [ppm][a]	^{232}Th C_{aw} ± 1SD [ppm] [a]	^{147}Sm C_{aw} ± 1SD [ppm] [a]	Distance to grain boundary [µm] [b]	in situ AHe date ± 1SD [Ma]
Ap-McClure_1	289	8.58×10^{15}	5.20×10^{15}	-	-	-	56	-
Ap-McClure_2	332	5.27×10^{15}	4.52×10^{15}	-	-	-	60	-
Ap-McClure_3	310	6.10×10^{15}	2.39×10^{15}	3.8 ± 0.4	16.9 ± 1.5	179 ± 27	63	236.8 ± 91.6
Ap-McClure_4	301	4.91×10^{15}	3.88×10^{15}	3.5 ± 0.3	16.5 ± 1.5	162 ± 20	66	202.8 ± 136.1
Ap-McClure_5	307	5.88×10^{15}	2.90×10^{15}	3.4 ± 0.4	16.1 ± 2.0	162 ± 12	68	244.4 ± 120.3

Ap-McClure_6	231	4.24×10^{15}	2.81×10^{15}	3.0 ± 0.3	15.1 ± 1.5	182 ± 43	71	196.8 ± 116.8
Ap-McClure_7	302	4.47×10^{15}	2.40×10^{15}	3.2 ± 0.4	15.8 ± 2.5	189 ± 28	74	195.7 ± 99.1
Ap-McClure_8	305	4.83×10^{15}	3.14×10^{15}	3.3 ± 0.4	16.8 ± 2.9	164 ± 5	74	201.0 ± 123.9
Ap-McClure_9	308	8.60×10^{15}	2.45×10^{15}	-	-	-	45	-
Ap-McClure_10	311	7.38×10^{15}	3.26×10^{15}	-	-	-	49	-
Ap-McClure_11	325	5.36×10^{15}	2.46×10^{15}	-	-	-	52	-
Ap-McClure_12	317	8.42×10^{15}	4.07×10^{15}	5.5 ± 0.8	26.8 ± 6.0	112 ± 8	56	218.3 ± 105.6
Ap-McClure_13	344	5.64×10^{15}	4.94×10^{15}	5.3 ± 0.6	26.6 ± 4.9	114 ± 23	59	160.5 ± 114.6
Ap-McClure_14	359	7.59×10^{15}	3.95×10^{15}	5.1 ± 0.4	26.1 ± 3.4	116 ± 37	63	39.8 ± 20.2
Ap-McClure_15	337	4.53×10^{15}	3.01×10^{15}	4.8 ± 0.5	24.9 ± 4.1	129 ± 31	66	130.6 ± 20.2
Ap-McClure_16	303	4.61×10^{15}	2.51×10^{15}	4.7 ± 0.9	25.1 ± 6.4	158 ± 13	70	134.4 ± 76.4
Ap-McClure_17	330	4.25×10^{15}	2.13×10^{15}	4.6 ± 0.9	25.0 ± 6.9	153 ± 12	73	126.4 ± 63.3
Ap-McClure_18	270	6.22×10^{15}	2.76×10^{15}	-	-	-	9	-
Ap-McClure_19	315	2.77×10^{15}	5.01×10^{15}	(3.2 ± 0.3)	(15.4 ± 1.9)	(151 ± 43)	24	152.8 ± 162.6
Ap-McClure_20	320	5.56×10^{15}	4.21×10^{15}	(3.7 ± 0.7)	(19.9 ± 5.1)	(178 ± 55)	39	200.0 ± 145.4
Ap-McClure_21	343	5.63×10^{15}	4.39×10^{15}	4.7 ± 0.9	25.8 ± 6.3	168 ± 30	54	162.6 ± 112.6
Ap-McClure_22	308	3.08×10^{15}	4.60×10^{15}	3.8 ± 0.6	19.4 ± 3.7	132 ± 24	65	133.1 ± 132.6
Ap-McClure_23	279	4.88×10^{15}	3.82×10^{15}	3.4 ± 0.4	16.2 ± 1.9	124 ± 13	49	202.8 ± 144.4
Ap-McClure_24	322	6.35×10^{15}	2.24×10^{15}	(3.4 ± 0.4)	(15.2 ± 1.8)	(128 ± 11)	35	274.1 ± 98.6
Ap-McClure_25	304	6.37×10^{15}	2.94×10^{15}	(3.5 ± 0.4)	(15.1 ± 1.5)	(131 ± 9)	19	265.8 ± 120.5
Ap-McClure_26	265	6.98×10^{15}	2.99×10^{15}	-	-	-	43	-
Ap-McClure_27	354	5.46×10^{15}	2.62×10^{15}	5.5 ± 1.0	26.4 ± 6.4	117 ± 12	60	142.6 ± 69.3
Ap-McClure_28	363	6.12×10^{15}	3.53×10^{15}	6.2 ± 0.8	30.5 ± 6.3	118 ± 5	74	139.8 ± 79.8
Ap-McClure_29	219	6.93×10^{15}	4.19×10^{15}	-	-	-	38	-
Ap-McClure_30	321	6.47×10^{15}	2.79×10^{15}	-	-	-	21	-
Ap-McClure_31	323	6.77×10^{15}	4.14×10^{15}	-	-	-	4	-
Ap-McClure_32	301	4.34×10^{15}	3.68×10^{15}	(3.2 ± 0.4)	(15.6 ± 2.6)	(140 ± 15)	36	194.0 ± 141.7
Ap-McClure_33	299	5.41×10^{15}	3.12×10^{15}	3.4 ± 0.4	16.5 ± 2.2	138 ± 22	52	230.0 ± 125.7

Ap-McClure_34	296	4.93×10^{15}	2.48×10^{15}	3.4 ± 0.3	16.4 ± 1.7	149 ± 31	68	202.1 ± 96.6
Ap-McClure_35	330	5.25×10^{15}	2.77×10^{15}	3.5 ± 0.4	15.8 ± 1.7	167 ± 12	50	211.9 ± 112.0
Ap-McClure_36	325	6.72×10^{15}	2.99×10^{15}	(3.2 ± 0.4)	(15.1 ± 1.5)	(128 ± 9)	34	296.1 ± 128.3
Ap-McClure_37	323	4.49×10^{15}	3.33×10^{15}	(3.8 ± 0.8)	(19.5 ± 5.9)	(127 ± 7)	18	168.2 ± 115.7
Ap-McClure_38	327	5.03×10^{15}	2.83×10^{15}	-	-	-	2	-

[a] Alpha-stopping distance weighted parent nuclide concentrations (C_{aw}; see Section 2.5) were not calculated for spots less than the maximum alpha-stopping distance of 40 µm away from the grain boundary, and for spots that were measured along a c-axis parallel traverse (Section 2.5). Note that locating the ^{4}He spots on the parent nuclide map is subject to uncertainty, especially for non-straight grain boundaries. Thus, the C_{aw} calculation for spots close to the grain rim needs to be treated with caution. Where the interpolated parent nuclide map adds area to the grain, C_{aw} values are reported in round brackets.

[b] c-axis orthogonal distance from the He-measurement spot centre to the nearest grain rim.

For Apatite-McClure in situ ^{4}He profiles are not displayed due to the ^{4}He measurements' high standard deviation (SD).

Appendix C: Apatite-BaF forward-modelled ^{4}He profiles

To assess how well the thermal history retrieved for Ap-BaF-P1 (Fig. 6) fits the entire grain Apatite-BaF, we forward-modelled the measured ^{4}He profiles that could not be inverted for thermal histories (Ap-BaF-P2 to Ap-BaF-P4) using the acceptable paths and best-fit path from Ap-BaF-P1 shown in Fig. 6d (Fig. C1). For Ap-BaF-P2, only a core-rim profile was measured. For display purposes, we modelled it as a c-axis symmetric profile (Fig. C1a). Ap-BaF-P4 is strongly asymmetric. We merge two core-rim profiles for forward-modelling at the grain centre (Section 2.6), leading to a significant jump in concentration (Fig. C1c).

Overall, the forward-modelled ^{4}He profiles based on results from Ap-BaF-P1 fit the measured profiles Ap-BaF-P2 to Ap-BaF-P4 reasonably well. The best-fit cooling history for Ap-BaF-P1 results in a misfit between the forward modelled and measured ^{4}He profiles of m=2.86 for Ap-BaF-P2, m=4.51 for Ap-BaF-P3, and m=4.27 for Ap-BaF-P4. The best-fit modelled profiles for each measured ^{4}He profile have misfits of m=2.32 (Ap-BaF-P2), m=4.13 (Ap-BaF-P3) and m=3.32 (Ap-BaF-P4). When the centre measurement is excluded from the misfit calculation for Ap-BaF-P2 and Ap-BaF-P4, the misfits improve to m=1.89 and m=1.77, respectively.

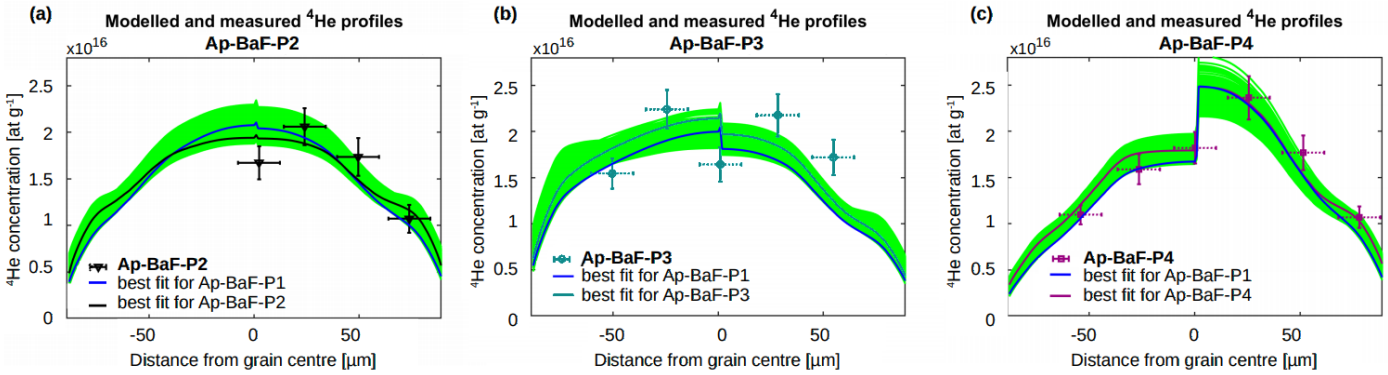

Figure C1: Forward models for Ap-BaF-P2 to Ap-BaF-P4. The ^{4}He profiles were forward-modelled based on the acceptable t-T paths of Ap-BaF-P1 (Fig. 6d). The modelled ^{4}He concentration in the centre of the grain jumps because the forward models merge two core-rim profiles (Section 2.6). Green profiles are based on acceptable paths that represent a GOF >5% (Fig. 6). The ^{4}He profiles with the lowest misfit m (Section 2.6, Eq.2) are highlighted in the respective measured profile's colour. The profile in dark blue is based on the best-fit path of Ap-BaF-P1 (see Fig. 6d).